NOAA Technical Memorandum

Cloud, Radiation, and Surface Forcing in the Equatorial Eastern Pacific

Jeffrey Hare
Christopher Fairall
Taneil Uttal
Duane Hazen
Meghan F. Cronin
Nicholas Bond
Dana Veron

November 2005

U.S. DEPARTMENT OF COMMERCE
National Oceanic and Atmospheric Administration

NOAA Technical Memorandum

Cloud, Radiation, and Surface Forcing in the Equatorial Eastern Pacific

Jeffrey Hare
Cooperative Institute for Research in Environmental Sciences
University of Colorado and NOAA/Earth System Research Laboratory
Boulder, Colorado

Christopher Fairall, Taneil Uttal, Duane Hazen
NOAA/Earth System Research Laboratory
Boulder, Colorado

Meghan F. Cronin
NOAA Pacific Marine Environmental Laboratory
Seattle, Washington

Nicholas Bond
Joint Institute for the Study of the Atmosphere and Oceans
University of Washington and NOAA/Pacific Marine Environmental Laboratory
Seattle, Washington

Dana Veron
Rutgers University
New Brunswick, New Jersey

Earth System Research Laboratory
Physical Sciences Division
Boulder, Colorado

November 2005

U.S. Department of Commerce
National Oceanic and Atmospheric Administration

NOTICE

Mention of a commercial company or product does not constitute an endorsement by NOAA/Earth System Research Laboratory. Use of information from this publication concerning proprietary products or the test of such products for publicity or advertising purposes is not authorized.

For sale by the National Technical Information Service, 5285 Port Royal Road
Springfield, VA 22061

Contents

Cloud, Radiation, and Surface Forcing in the Equatorial Eastern Pacific

Jeffrey Hare, Christopher Fairall, Taneil Uttal, Duane Hazen, Meghan F. Cronin, Nicholas Bond, and Dana Veron

ABSTRACT. Cloud and surface flux processes play an important role in defining sea surface temperature in the tropical eastern Pacific Ocean. The need to increase our knowledge of air-sea interaction in this region has led to the refinement and deployment of the enhanced Tropical Atmosphere-Ocean Eastern Pacific Investigation of Climate (TAO-EPIC) buoys in that region and the development of the Pan-American Climate Studies (PACS) program. In conjunction with these efforts, we developed and implemented a regular and repeated ship-based cloud and flux measurement program onboard the NOAA Ships *Ronald H. Brown* and *Ka'imimoana*. These intensive measurement campaigns were made during NOAA's fall (*Ronald H. Brown*; 1999–2002) and spring (*Ka'imimoana*; 2000–2002) maintenance cruises along the 95W and 110W TAO buoy lines. With this dataset, we have developed a limited climatology of the PACS area, and we continue to repeat the deployments during the fall cruises to the TAO lines. The analysis presented shows seasonal (spring vs. fall) contrasts in the latitude averaged variables.

At a given latitude, the year-to-year and seasonal variabilities of many of the meteorological and oceanic means are relatively small. However, we find notable seasonal variability in the northern branch of the Inter-Tropical Convergence Zone (ITCZ), the north-south sea surface temperature gradient, and heat fluxes north of the equator. In the fall, the strengthening of the north-south SST contrast enhances convective activity (more and deeper clouds, precipitation, southerly inflow) in the area around 6N, 95W; diurnal variations of low cloud fraction were weak. In contrast, the spring clouds varied significantly over the diurnal cycle with substantially lower cloud fraction during the day south of 5N. This may be a result of greater subsidence or surface heating during the day. Relatively low average cloud base heights around the equator are due to decoupling of the marine boundary layer (MBL) as southerly air flows over the region of the cold tongue. In the fall, the cold tongue surface water is significantly cooler, corresponding with very low and evenly distributed cloud base observations.

Estimates of cloud forcing of surface radiation in the visible and infrared (IR) are presented. In the IR, cloud forcing strongly correlates with cloud fraction and IR cloud forcing shows significant seasonal variability. In the solar band, less variability in seasonal cloud forcing was seen. From the observations, it is determined that clouds in the eastern equatorial Pacific tend to cool the surface by about 40 Wm^{-2} in both seasons.

The spring net heat flux is nearly symmetrical about the equator with a maximum (175 Wm^{-2}) at the equator decreasing to about 100 Wm^{-2} at 10N and 8S. The equatorial maximum is associated with lower turbulent fluxes and modestly lower cloudiness at the equator. In the fall, the maximum net heat flux (180 Wm^{-2}) is at 2S and the minimum (essentially zero) is at 6N. Much of the fall net heat flux asymmetry is caused by cloud radiative forcing.

1. INTRODUCTION

1.1. Background

Accurate estimates of the turbulent and radiative fluxes at the surface are required for virtually all aspects of atmospheric boundary layer research, model validation, and assessment of air-sea interactions. The importance of the turbulent fluxes can be profoundly illustrated in the investigation of Miller et al. (1992), where a small change in the bulk flux parameterization in the European Center for Medium-Range Weather Forecasts (ECMWF) model completely changed the modeled climate of the tropics. Recent studies with the Community Climate Model (CCM3) have shown the clear need for improvements in the representation of turbulent (Collins et al. 1997) and radiative fluxes (Wild et al. 1995; Garratt and Prata 1996). Of course, the variability of radiative fluxes at the surface is dominated by clouds, and a major source of uncertainty in General Circulation Models (GCM) is the representation of clouds and their interactions with the surface radiative field (Cess et al. 1995; Browning 1994).

Marine boundary layer (MBL) clouds strongly influence global climate. Unlike the ocean surface, they present a relatively high albedo, which reduces the flux of solar radiation to the surface. In addition, the relatively low altitudes of MBL clouds provide marginal impacts on upwelling infrared flux (Randall et al. 1984). Clouds also couple directly to the surface fluxes through the winds and scalar fields (e.g., Stevens et al. 2001). The optical properties of MBL clouds are determined by the balance of surface evaporation, entrainment and radiative cooling combined with the boundary layer aerosol profiles (Albrecht 1989; Menon et al. 2002). Aerosols influence the size distribution of MBL cloud droplets, which in turn affect solar radiative interactions and drizzle production (Albrecht 1993; Zhu and Albrecht 2002). Coupled ocean-atmosphere processes in the tropics and subtropics are significantly influenced by MBL stratocumulus and trade cumulus clouds. In the tropics, clouds generated by deep convection dominate in some regions (for example, in the western Pacific), while MBL clouds are more prevalent in other areas.

As the breeding ground of the American monsoon system and a key region for El Niño, the tropical eastern Pacific is considered a critical area for accurate estimation of short-term climate variability. Coupled model studies show that the radiative effects of MBL clouds are essential in producing the observed equatorial cold tongue sea surface temperature structure (Philander et al. 1996; Li and Philander 1996; Delecluse et al. 1998). This includes the classical subtropical stratocumulus regimes off the coasts of California and Peru and the equatorial stratocumulus occurring in the region of strong north-south sea surface temperature (SST) gradient around latitudes 85–110W. Except for some notable exceptions (Bond 1992; Yuter and Houze 2000; Hashizume et al. 2003), direct observations of air-sea interaction processes in this region are rare.

1.2. The NOAA Climate Monitoring Program

As discussed above, air-sea fluxes, clouds, and other MBL processes that influence flux variability are a major focus of the NOAA Climate Variations (CLIVAR) Pan American Climate

Studies (PACS) and the Eastern Pacific Investigation of Climate Processes in the Coupled Ocean-Atmosphere System (EPIC). The CLIVAR observational strategy includes a combination of short-term, comprehensive process studies, coupled with oceanographic and meteorological monitoring studies (Weller et al. 1998; Smith et al. 2001; Esbensen et al. 2002). The Tropical Ocean Atmosphere (TAO) buoys and specialized Ocean Reference Stations (ORS) are the primary continuous in situ air-sea flux measurement platforms. The ORS are large discus buoys designed to obtain high-quality bulk data for estimation of air-sea fluxes. These buoy data are critical in the evaluation of fluxes for various climate regimes (McPhaden et al. 1998), for intercomparison of operational forecast models (Josey et al. 2002), and for several efforts to retrieve fluxes from satellite information (Jones et al. 2001; Project SEAFLUX http://paos.colorado.edu/~curryja/ocean/, [Curry et al. 2004]).

The use of networks such as the TAO and ORS buoys is not expected to meet all air-sea flux scientific needs (Taylor 2001; Cronin et al. 2002). There are some practical limitations associated with the current buoy system technology, including insufficient accuracy, coarse spatial representation, and lack of atmospheric profile information. For example, the change in air-sea heat flux associated with a doubling of atmospheric CO_2 concentration is a few Wm^{-2}, and for accurate representation of seasonal time scales, the air-sea fluxes need to be constrained within 10 Wm^{-2} (Webster and Lukas 1992). These sensitivity requirements are unlikely to be met with long-term monitoring buoys such as TAO. This is not surprising, as air-sea interaction buoys must operate unattended for 6–12 months, and it is therefore necessary to compromise accuracy for durability and cost. From these platforms, turbulent fluxes are typically not measured directly but are estimated using bulk flux routines (Fairall et al. 1996a, 2003). Finally, instruments for monitoring atmospheric profiles (wind profilers, sodars, etc.) typically require more power than is practically available on most buoys.

Atmospheric profile information and direct flux measurements are critical for interpretation of surface data, for comparison with operational weather models, and for improved satellite retrievals. Thus, buoy observations must be supplemented with high-quality flux and profile measurements from CLIVAR intensive field programs, such as EPIC2001 (Raymond et al. 1999, 2004; Bretherton et al. 2004), and other monitoring efforts (Weller 1998; Taylor 2001; Esbensen et al. 2002). Part of this strategy includes the PACS/EPIC enhanced monitoring program (Cronin et al. 2002) which provides additional buoys on the 95W TAO line, additional sensors on existing buoys, and a program of comprehensive flux and cloud measurements from the twice-yearly research vessel cruises to service the 95 and 110W buoy lines (see Figure 1).

1.3. Scope of This Paper

In this paper we present an analysis of the first three years of measurements from the ship-based component of the enhanced monitoring program. The NOAA Environmental Technology Laboratory (ETL) and the NOAA Pacific Marine Environmental Laboratory (PMEL) cooperated in implementing the program beginning in 1999 (see section 2). Details on the ship-based flux and cloud property measurements are given in section 3. The emphasis of the present analysis is on cross-equatorial variability of the mean surface fluxes, the near-surface meteorology, and simple cloud properties (section 4), contrasting the spring and fall seasons. Following a discussion of cloud radiative forcing (section 5) and clear-sky radiative flux models

(section 6), we present a similar cross-equatorial analysis of mean cloud properties and cloud forcing (section 7). Conclusions are given in section 8.

2. THE PACS/EPIC ENHANCED MONITORING CRUISES

During the twice-yearly maintenance cruises along the 95W and 110W TAO buoy lines, we implemented a ship-based cloud and flux measurement program to obtain statistics on key surface, MBL, and low-cloud macrophysical, microphysical, and radiative properties. These deployments on the NOAA Ships *Ka'imimoana* and *Ronald H. Brown* serve to enhance the regular monitoring measurements from the TAO buoys. While not comprehensive, these data are useful for coupled ocean-atmosphere modeling efforts, for MBL and cloud modeling, and to improve satellite retrieval methods for deducing MBL and cloud properties on larger spatial and temporal scales.

The primary objectives of our ship-based efforts were to:

- Increase the utility of long time series buoy observations of air-sea flux bulk input variables through instrument intercalibration, supplemental atmospheric profiles, measurements of cloud properties, and the addition of spatial context;

- Provide comprehensive information for operational weather forecast model evaluation/development and satellite calibration/validation and retrieval algorithm development;

- Advance the development of bulk turbulent and radiative flux parameterizations either directly or by establishing links with MBL numerical modeling research efforts;

- Advance our understanding of the role of MBL clouds, aerosols, and drizzle in cloud radiative forcing.

2.1. Methodology

The southern end of the 95W line is in the subtropical stratocumulus belt off the west coast of South America, and the 110W line is at the western edge of the PACS region. The northern and southern branches of the Inter-Tropical Convergence Zones (ITCZ) cross the TAO buoy lines at approximately 8-10N and 5-8S latitudes, respectively. During the Northern Hemisphere spring (from hereon, reference to seasons will be for the Northern Hemisphere), the southern branch of the ITCZ is much weaker than the northern arm and is essentially nonexistent in the fall. For example, examination of the rainfall displayed in Figure 2 reveals the branched structure of the ITCZ in the spring and also shows the distinct change in rainfall climatology between the seasons. The equatorial cold tongue is well developed at both longitudes, and persistent low stratocumulus and occasional fog are encountered in this area.

Two portable flux measurement packages have been developed that can be installed on either ship. The systems include instruments capable of making observations of air-sea turbulent and radiative fluxes, along with ceilometer measurements of cloud base, and rawinsonde profiles of wind, temperature, and humidity. On some of the cruises, the NOAA ETL cloud radar (Ka-band) and multi-channel microwave and infrared radiometer systems were also deployed. Other cruises included an S-band or 915-MHz vertically-pointing clear air radar. Details of these deployments are provided in section 3. The supplemental remote sensing instruments allow for the computation of low-cloud statistics (integrated liquid water content, cloud base height, and fraction) along with the complete surface energy budget of the oceanic and atmospheric boundary layers which are provided from the flux system.

We completed seven measurement missions between fall 1999 and fall 2003. The fall 2001 period included the regular TAO-PACS measurement deployment plus the EPIC2001 field program (Raymond et al. 2004). Each mission includes transects of the 95W and 110W buoy lines between 8S and 12N, along with transit legs to and from the experimental area.

2.2. Database

For the analysis presented in this paper, data time series from the flux system, cloud ceilometer, and microwave radiometer are processed to 10-minute time resolution and integrated to a common time format. The flux database includes turbulent and radiative fluxes and all relevant near-surface bulk meteorological variables. The ceilometer cloud base height information is processed to 10-min cloud statistics including vertical cloud fraction and 15%, 50% (median), and 85% heights for the cloud base cumulative distribution. The microwave radiometer data include column integrated water vapor (*IV*) and integrated liquid water content (*W*). We have created a web-accessible database for our PACS collaborators and other EPIC investigators. Data are archived for public use at ftp://ftp.etl.noaa.gov/user/cfairall/EPIC/epicmonitor/. The present status of the processed data is given in Table 1.

Table 1. Present processed data availability at the ETL PACS ftp site.
D — data available on site; I — image files only; X — available but not posted.

Mission	Flux	Radar profiler	Ceilometer	MWR	Sonde	Cloud radar	C-band radar
Fall 1999	D	I	D	D	D	N/A	X
Spring 2000	D	X	D	D	D	N/A	N/A
Fall 2000	D	X	D	D	D	I	I
Spring 2001	D	X	D	D	D	N/A	N/A
Fall 2001	D	X	D	D	D	D	X
Spring 2002	D	X	D	D	D	N/A	N/A

3. MEASUREMENTS

All PACS cruises in this analysis included the ETL flux system and a basic cloud monitoring package, which includes a 915-MHz wind profiler or S-band radar, GPS rawinsondes, a cloud ceilometer, and an automated two-channel microwave radiometer (White et al. 1995; Fairall et al. 1997). On two cruises we also fielded the NOAA Portable Cloud Observatory (NPCO), which features the 35-GHz cloud radar (Moran et al. 1998), a two-channel microwave radiometer (Snider and Hazen 1998), and an upward- looking IR radiometer. The NPCO gives much more detail on cloud properties (vertical distribution of liquid water, cloud droplet sizes, etc). A list of the instruments is shown in Table 2, where items 11–13 constitute the NPCO. When operating on the *Ronald H. Brown,* we also have made use of the permanent scanning C-band Doppler radar, which provides detail on the spatial distribution of convection, precipitation, and clouds (Peterson et al. 2002).

Table 2. Instruments deployed and measurements by ETL for the ship-based cloud/MBL monitoring project.

Item	System	Measurement
1	Motion/navigation package	Motion correction for turbulence
2	Sonic anemometer/thermometer	Direct covariance turbulent fluxes
3	IR fast H_2O/CO_2 sensor	Direct covariance moisture/CO_2 fluxes
4	Mean SST, air temperature/RH	Bulk turbulent fluxes
5	Pyranometer/Pyrgeometer	Downward solar and IR radiative flux
6	Ceilometer	Cloud base height
7	0.92- or 3-GHz Doppler radar profiler	Cloud top height, MBL microturbulence
8	Rawinsonde	MBL wind, temperature, humidity profiles
9	23, 31 GHz :wave radiometer (ARM type - MAILBOX)	Integrated cloud liquid water Integrated total water vapor
10	BNL rotating shadowband radiometer	Direct/diffuse solar
11	35-GHz Doppler cloud radar	Cloud microphysical properties
12	20, 31, 90 GHz :wave radiometer (ETL)	Integrated cloud liquid water Integrated total water vapor
13	Upward pointed IR thermometer	Cloud base radiative temperature
14	*Ronald H. Brown* C-band radar	Precipitation spatial structure

3.1. Near-Surface Bulk and Flux Data

The ETL flux group has spent over 15 years developing techniques for accurate ship-based measurements (Fairall et al. 1996a, 1997, 2003). Mean wind speed and high- frequency turbulent wind component fluctuations are measured with a sonic anemometer with full motion corrections (Edson et al. 1998). We also correct for mean flow distortion by the ship's structure based on computational fluid dynamics (CFD) calculations with empirical tuning (Yelland et al. 1998). The CFD calculations have been performed on the modeled profile of the *Ronald H. Brown* and the R/V *Knorr* (Woods Hole Oceanographic Institution; WHOI). Because of the physical similarities of the ships, the *Knorr* CFD results have been applied to the *Ka'imimoana* dataset. The downwelling radiative flux sensors are Eppley precision pyranometers (PSP - solar flux) and precision infrared radiometers (PIR - IR flux), and these instruments are calibrated at the factory and are cross-calibrated against the Department of Energy's Brookhaven National Laboratory (BNL) system deployed on the *Ronald H. Brown* (Miller et al. 2004). The near-surface ocean temperature (SST) is measured with a specially developed floating temperature sensor (called a "seasnake") which samples at a depth of about 5 cm. This sensor fully resolves all diurnal warm layers, while the true interface temperature is obtained by subtracting a cool-skin correction (Fairall et al. 1996b). During cruises on the *Ronald H. Brown*, the modeled cool skin is routinely checked for quality against the University of Washington Applied Physics Laboratory (APL) radiometric skin temperature measurements (http://cirims.apl.washington.edu/). Mean air temperature and relative humidity are measured with aspirated Väisälä HMP-235 sensors and cross-calibrated with the resident WHOI Improved Meteorology (IMET) systems onboard the NOAA ships. The sonic anemometer/thermometer, a fast-response infrared hygrometer, and a high-speed open-path infrared H_2O/CO_2 sensor are used to make measurements of turbulent fluxes. The direct covariance and inertial-dissipation fluxes are computed at 10-min and 1-hr time intervals, and bulk turbulent fluxes are computed with version 3.0 of the COARE bulk flux algorithm (Fairall et al. 2003).

3.2. Standard Cloud Data

A Väisälä infrared laser ceilometer (model CT25K) provides a measurement of the cloud base height every 30 seconds, and cloud cover statistics are computed over the course of the day from these measurements. Atmospheric profile observations of wind speed and turbulence within the lowest few kilometers are made with the 915-MHz wind profiler on the *Ronald H. Brown* (Ecklund et al. 1988, 1999). From the profile of clear-air backscatter intensity, this instrument also provides an estimate of MBL depth in almost all conditions (White et al. 1995). For boundary layer clouds, this is equivalent to cloud top height. All cruises featured continuous observations of total column atmospheric water by an automated microwave radiometer using a Radiometrics Inc. system of the type developed for the Atmospheric Radiation Measurements (ARM) program (Liljegren et al. 2001). This instrument makes use of standard two-channel (23- and 31-GHz) measurements of microwave brightness temperature which are inverted to give information on column integrated water liquid and vapor path.

3.3. NOAA Portable Cloud Observing (NPCO) System

The NPCO is comprised of a 35-GHz vertically-pointing Doppler radar, a multiple-channel microwave radiometer (20.6- and 31.65-GHz), and a multiple-channel infrared radiometer (9.9–11.4 or 10.6–11.3 micrometer). Matrosov et al. (1995) and subsequent papers have outlined methods for deriving microphysical quantities of cirrus clouds using these instruments. Frisch et al. (1995, 1998, 2002) and subsequent papers by various authors have discussed methods to combine the data from these systems to deduce profiles of cloud droplet size, number concentration, and liquid water concentration in MBL clouds.

3.4. Accuracies

The fundamental air-sea flux variables (sensible and latent turbulent heat fluxes, net solar flux, and net IR flux) are each measured to about 5 Wm^{-2} for time averages of duration greater than a few days (Fairall et al. 1997, 1998). For similar averaging times, air and sea surface temperature are accurate to ±0.2 C; air and surface specific humidity to an accuracy of ±0.3 gkg^{-1}; true wind speed to about ±0.2 ms^{-1}. More detailed error analysis of the flux system can be found in Fairall et al. (1996a, 2003). The ceilometer has a vertical resolution of 15 m, but its accuracy is difficult to characterize because, to some extent, it depends on the definition of cloud base and its extraction from the profile of laser backscatter intensity (the bottoms of clouds may be indistinct). Microwave retrievals of water vapor are accurate to about 5% with a variable bias of ±0.1 cm, while retrievals of liquid water are accurate to about 10% with a variable bias of ±50 gm^{-2} in the Tropics (Westwater et al. 2003). The poor performance for liquid water in the Tropics is a result of the combination of the radiometers' increasing sensitivity to water vapor with temperature and decreasing sensitivity to liquid water with temperature. Tropical MBL clouds have cloud liquid water path (W) values on the order of 100 gm^{-2}, and this bias presents a particular problem for estimation of atmospheric water vapor. We have attempted to correct for this by removing from the raw W signal a time-interpolated bias determined using the ceilometer to find cloud-free periods ($W = 0$). During broken cloud periods this has been quite effective, but the method is not successful for long, solid cloud periods.

4. CROSS-EQUATORIAL AND SEASONAL DEPENDENCE OF OCEAN FORCING AND CLOUD PROPERTIES

In this section, we examine the processed datasets from the first seven cruises in the PACS region. By definition, a "climatology/monitoring" project implies multiple measurements in the same region to evaluate variability. In this region, the long term environmental variability is dominated by El Niño/La Niña cycles, but in three years of investigations reported here, it is possible to observe only a portion of one cycle. There are significant seasonal differences between our spring and fall cruises. There is also some difference between the 110W and 95W transects. Finally, there is short-term variability associated with the Madden-Julian oscillation, synoptic-scale fluctuations such as easterly waves, and the Tropical Instability Waves (TIW) in the ocean that cause latitudinal displacements of the SST fronts. An example of the SST and wind fields obtained from the ECMWF model for both seasons is shown in Figure 3. In the remainder of this section we will show various quantities of interest computed as one-day

averages and averaged further in latitude bins. One-day averages are chosen as a convenience that removes the diurnal cycle and reduces much of the sampling variability. There are some differences in the average properties at 95W and 110W, but the seasonal variations dominate. As a result, we have combined 95W and 110W data in the following presentation.

4.1. Meteorological Variables and Fluxes

In Figure 4a, we show an example of the wind components for each cruise to illustrate the variability at daily time scales. Figure 4b shows the same data averaged by season: strong southeasterly winds occur south of the equator with a minimum in the easterly component well north of the equator and a clear strengthening of the northerly component approaching the ITCZ in the fall. Wind speed is a maximum (about 7 ms^{-1}) at the southern end of the study area with a tendency for the spring winds to be stronger.

We have computed the standard deviations of the ensemble daily averages of the environmental variables within each latitude/seasonal bin. The results show small latitudinal variations, which we have summarized in Table 3. The sampling uncertainty at a given bin/season is the standard deviation divided by the square root number of samples (typically 5–10). Thus, the uncertainties in the individual *mean* values shown in Figure 4b and the related plots to follow are the standard deviations given in Table 3 multiplied by approximately one-third.

Table 3. Standard deviation of selected variables, computed for all three years of cruise data during each season (spring or fall) within a single latitude bin. The values presented are the average variance of all latitude bins.

Variable	Symbol	Units	Fall Σ	Spring Σ	Measurement Height
Wind speed	S	ms^{-1}	2.5	2.5	17.5 (*RB*) / 16.5 (*KA*) m
N. wind component	U_n	ms^{-1}	1.5	1.4	17.5 (*RB*) / 16.5 (*KA*) m
E. wind component	U_e	ms^{-1}	2	2	17.5 (*RB*) / 16.5 (*KA*) m
Air temperature	T_a	C	0.77	0.42	14.8 m
SST	T_s	C	0.92	0.57	-20 cm
Specific humidity	q	$g\ kg^{-1}$	0.65	0.7	14.8 m
Downward solar flux	R_{sd}	Wm^{-2}	56	27	N/A
Downward IR flux	R_{ld}	Wm^{-2}	14	9.3	N/A
Clear sky solar flux	R_{scl}	Wm^{-2}	14	14	--
Clear sky solar flux	R_{lcl}	Wm^{-2}	6.5	3.8	--
Sensible heat flux	H_s	Wm^{-2}	2.8	3.5	17.5 (*RB*) / 16.5 (*KA*) m
Latent heat flux	H_l	Wm^{-2}	24	20	17.5 (*RB*) / 16.5 (*KA*) m
Cloud fraction	f	-	0.2	0.14	N/A
Cloud base height	z_b	m	190	180	N/A
Precipitable water	IV	cm	0.89	0.61	N/A

In Figure 5, we show plots of the latitudinal distribution of air temperature (T_a) and SST (T_s). Note that the seasonal SST cycle is strongest (about 6 C) at the equator and further south, and becomes negligible to the north at about 10N. The strong seasonal variation in SST is not mirrored in the latitudinally-averaged sea-air temperature difference (Figure 6), which is an indication of the boundary layer adjustment processes. There is a slightly positive minimum in sea-air temperature difference (T_s-T_a) at or just south of the equator. The maximum in T_s-T_a (about 2.0 C in the fall) occurs at 5N, which is well downwind of the prevalent SST front around 2–3N. From Figure 6, we see that a relatively strong residual T_s-T_a exists in the fall. This indicates that the surface forcing is greater in the fall, and that the MBL response to the surface forcing is not rapid enough to reduce the sea-air temperature difference such as is seen in the spring. Because T_s-T_a is the result of a dynamic balance between surface fluxes, entrainment, and radiative fluxes, it is difficult to explain this response quantitatively without a detailed model study. The boundary layer moisture pattern (as defined by specific humidity and column water vapor) is closely coupled to SST and is shown in Figure 7. Total column water vapor (Figure 7b) actually shows a much stronger seasonal variation (i.e., a factor of 2 versus about 30% for MBL moisture). The upper air is much drier south of about 2N during the fall, presumably because of the overpowering influence of deep convection in the northern ITCZ. This has important implications for cloud top IR radiative cooling.

The latitudinal means of surface sensible and latent heat fluxes are shown in Figure 8. The turbulent fluxes have minima at, or just south of, the equator, with significantly lower sensible heat fluxes occurring during the spring. Negative sensible heat fluxes are observed episodically, but the overall average is slightly positive. The strong MBL response north of the equator in the fall is the combined result of the greater sea-air temperature difference, accelerating winds, and the large change in hydrostatic stability. Naturally, solar forcing is stronger north of the equator in the spring (approaching summer) and south of the equator in the fall (approaching winter). This effect is somewhat masked by the relatively large cloud forcing effects (Figure 9), but the solar forcing is apparent in the clear-sky fluxes (see section 6). The northern ITCZ is readily apparent as decreased net solar and increased net IR flux around 5–8N during the fall season. The precipitation (Figure 10) is most likely undersampled due to the effects of ship flow distortion on the in situ sensor catchment (Yuter and Parker 2001), but the strong northern ITCZ in fall (north of 6N) and the double ITCZ structure in the spring (at approximately 4N and 4S) are apparent. The peak values correspond roughly to the TRMM maps in Figure 2. However, the TRMM fall map puts the precipitation maximum around 8N, which corresponds more closely with the radiative flux than the precipitation measured on the ship.

4.2. Cloud Properties

The low cloud fraction (Figure 11) data show the large convective cloud masses in the fall associated with the most active phase of the ITCZ, and the location of the peak corresponds well with the radiative results in Figure 9. The southern ITCZ in spring is also clearly seen at 5S, but there seems to be little evidence near 8S of the expected fall increase in cloudiness associated with the edge of the Peruvian stratocumulus region (Norris and Leovy 1994). As displayed in Figure 11, the 12-hr (day) and 24-hr cloud fraction are plotted separately as a simply indication of regions with diurnal variation in cloud fraction. Stratocumulus MBL clouds tend to

decrease in the local afternoon in response to solar heating, while trade cumulus clouds tend to increase in response to strong surface evaporation and instability. The results in Figure 11 are somewhat unanticipated, with only the spring data away from the southern branch of the ITCZ showing significant daytime suppression of marine clouds. This suggests that in the spring the clouds outside the ITCZ are more stratocumulus-like or that the subsidence in those regions has a strong diurnal cycle with an afternoon maximum.

Fair weather broken cumulus clouds are nearly ubiquitous in the undisturbed tropical MBL, and they appear to be part of a self-regulating system that produces low cloud base heights around 600 m with astoundingly little variation. However, averaging cloud base heights can disguise this, as when tilted trade cumulus clouds are present in the field. In this case, the ceilometer may return high-biased values for "cloud base" which are actually the tilted sides of the clouds. Also, in the presence of deep convection there are often outflow clouds at intermediate heights. Thus, a simple average tends to be biased toward higher values than the actual MBL cloud bases (Figure 12). We have started our processing with the time series of base heights from the cumulative distribution where 15% of the samples in a 10-min time window are lower than the selected height, as the 15% distribution height tends to reduce the influence of tilted clouds. Figure 12 shows the mean of these heights, which suggests seasonal differences only in the northern region. However, a more enlightening approach is to examine the probability distribution of base heights and look for the peak. In this case, we find a peak at 600 m for most latitudes during both spring and fall seasons. There is typically a secondary peak between 1000–1500 m caused by convective cloud top horizontal spreading at the height of the inversion. Exceptions to the common 600 m warm convective cloud base arise for cloud base heights at about 500–550 m in the core of the ITCZ and when double-peaked distributions (450 and 600 m) occur within 2 degrees of the equator (see lower panel on Figure 12). Example distributions for a typical southern hemisphere spring latitude bin (5S to 7S) and about the equator (1S to 1N) in the fall are shown in Figure 13. The slightly lower cloud bases in the ITCZ reflect higher relative humidity in the convective regions. The additional lower bases near the equator are caused by increased stratification associated with the atmospheric flow onto the cold tongue. In the case of the equator during fall, the cloud base height distribution has no dominant peak, but instead is essentially flat from 100 to 800 m. This implies stronger surface layer stability and decoupled boundary layers.

Measurements of time-averaged cloud liquid water path are shown in Figure 14a. Dividing these values by cloud fraction (Figure 11) gives us the mean W when clouds are present (Figure 14b), which provides a clearer representation similar to the "cloudy pixel liquid water" in satellite W retrievals. The higher W values (300 gm^{-2}) associated with the northern ITCZ are similar to those given by Weng et al. (1997). South of 3N we see the much lower W values (20–120 gm^{-2}) for stratocumulus/trade cumulus clouds. The average for fall is 45 gm^{-2}, and for spring it is 70 gm^{-2}.

5. CLOUD RADIATIVE FORCING

Cloud forcing (CF) provides an indication of the impact of clouds on the surface energy budget, and this analysis demonstrates the particular emphasis of our observations in the PACS/EPIC region. Cloud forcing is the difference in the observed mean radiative flux versus what the flux would be in the absence of clouds:

$$CF_x = < R_x > - < R_{x0} >, \quad \textbf{(1)}$$

where R is the radiative flux, the subscript $x = s$ for solar or $x = l$ for longwave (IR), and the subscript 0 refers to the clear-sky flux. A related variable that is often used is the *maximum* cloud forcing, which is the conditional change in the flux when a cloud is actually present:

$$MCF_x = < R_{x1} > - < R_{x0} > \approx \frac{CF_x}{f}, \quad \textbf{(2)}$$

where R_{x1} is the radiative flux for overcast conditions and f is cloud fraction. CF averages clear and cloudy periods, but MCF is the difference between overcast (cloud fraction, $f = 1.0$) and clear ($f = 0$) conditions. MCF is related to the radiative properties of individual clouds and can, in principle, be directly computed from microphysical and radiative variables, while CF is strongly dependent on whether it is cloudy or not. MCF also is applied in simple models that use cloud fraction to estimate cloud effects on radiative fluxes (see section 7). For this paper, we will use the CF of the *net* surface flux, which is the quantity most relevant to the surface heat balance of the ocean. Net CF is downward flux multiplied by 1- α (where α is albedo, and is estimated at 0.945 for solar wavelengths over the sea) or multiplied by the broadband IR emissivity (ε) of seawater (estimated as 0.97; Fairall et al. 1996a).

CF has seen extensive application as an index of the importance of clouds for the global heat balance (e.g., Ramanathan et al. 1995 for the Tropics; Walsh and Chapman 1998 for the Arctic). CF yields valuable information about cloud dynamics (Pincus et al. 1997) and is an important tool for diagnosing GCM treatments of cloud/radiative processes. Ramanathan et al. (1995) showed a direct link between surface cloud forcing (SCF) and oceanic dynamics. Furthermore, Tian and Ramanathan (2002) have shown that CF is much more directly linked to atmospheric regional dynamics and moisture transports than, say, surface turbulent fluxes.

Cloud forcing (CF) can be inferred globally using satellite data at the top of the atmosphere (TOA, Ramanathan et al. 1989), and it can be determined more indirectly from surface data. For SCF, the surface-based methods are more direct and more accurate, but provide limited sampling. Previous studies in the tropics have shown that the heavy water vapor burden in the boundary layer partially masks the longwave (LW) signal from clouds, and SCF is dominated by the solar flux, as LW SCF is about 5 to15 Wm^{-2} while shortwave (SW) SCF ranges from -50 to -90 Wm^{-2} (Stephens and Webster 1981). In subtropical stratocumulus regimes, the solar component is more nearly balanced by the LW component and the total SCF is perhaps closer to -30 Wm^{-2}.

This SW versus LW compensating effect depends strongly on latitude and season, and this balance is illustrated in Figure 15. Here we show a schematic CF phase diagram where LW CF and SW CF are used as X-Y axes in a cloud forcing climate region phase diagram. The plotted points represent averages from eleven ETL cruises in the tropics (Nauru99, four COARE cruises, JASMINE, two KWAJEX cruises, one PACS cruise, and CSP). Note that tropical regions have the strongest solar cloud forcing, while polar areas tend to have the strongest relative IR cloud forcing. In the upper midlatitude storm track, total SCF tends to be small because the solar and IR components approximately cancel.

6. CLEAR-SKY RADIATIVE FLUX PARAMETERIZATIONS

Radiative fluxes are used in meteorological models in a manner similar to turbulent fluxes, as profiles of the fluxes are converted to flux divergences for local heating or cooling rates. This requires complex radiative transfer codes to incorporate the absorption and scattering properties of the atmosphere (temperature, humidity, ozone, carbon dioxide, aerosols, and clouds), and the required accuracies are within a few Wm^{-2}. Clouds offer considerable modeling difficulties in the IR, but the impediments to accurate modeling are more severe in the solar band. A variety of state-of-the-art radiative transfer models (e.g., Mlawer et al. 1997, 2000) are available to estimate both IR and solar downward fluxes in clear-sky conditions. In this study we are concerned with radiative fluxes at the air-sea interface, so we can use simpler models that require less information. While the PACS cruises include radiosonde profiles and basic cloud information, we are also interested in related applications for buoys or data from ships of opportunity. These datasets are usually limited to measurements of near-surface meteorology, but supplemental information can be obtained from many research ships, such as visual observations of cloud cover.

A variety of simple parameterizations are available to estimate both IR and solar downward surface fluxes in cloud-free conditions. Upward fluxes are estimated through specification of interface temperature and an emissivity for IR flux or albedo for solar flux. Algorithms based on near-surface air temperature and humidity are effective for estimation of downward IR flux over the ocean, although regional or latitudinal adjustments are usually required. Clear-sky downward solar flux algorithms must account for the diurnal motion of the sun as a function of latitude and time of year. There have been a number of reviews of this class of radiative flux parameterizations (e.g., Lind and Katsaros 1984, Katsaros 1990; Key et al. 1996), so we will limit our specific comments to ones we used or considered.

The effects of clouds represent the greatest challenge for parameterizing surface radiative fluxes. A specification of *cloud fraction* is often sufficient to define most of the variability in IR flux associated with clouds. True cloud fraction is the instantaneous fraction of the sky covered by clouds and is usually determined by observers or whole-sky imaging devices. This is distinct from vertical cloud fraction, f, which is typically determined from time or space averages of vertically-oriented, narrow field-of-view sensors such as a cloud ceilometer or microwave radiometer (Berg and Stull 2002). For solar flux, more information is usually required, depending on the desired time resolution, including solar zenith angle, cloud thickness or aspect ratio, and cloud liquid water. A statistical representation of the variability of downwelling solar

flux is also a significant problem in models. For longer time scales or larger spatial scales, the simple statistical representations are somewhat better. It is also difficult to develop and/or verify parameterizations using point measurements. Thus, a solar flux parameterization developed from a month of data taken in the Bahamas may not be applicable at another location (or even for another time in the Bahamas). Still, some success has been obtained with parameterizations of *daily-average* solar flux, a quantity of use in many climate applications.

For the study of SCF, the realization of the fluxes at the air-surface interface can be handled effectively by these simpler methods. For one thing, we only require estimates of *clear-sky* flux because the all-sky flux is directly measured. Furthermore, we can accommodate regional and seasonal variability by tuning the model to fit the observations during clear periods. For this approach, the challenge is to plainly identify the clear periods. To do that, we use estimates of the vertical cloud fraction from the ceilometer data.

6.1. IR Flux

Most IR parameterizations estimate the flux in terms of near-surface parameters such as air temperature (T_a). For example, a specification of downward IR flux may be written:

$$R_{ld} = \varepsilon_e \sigma T_a^4 \ , \qquad \textbf{(3)}$$

where ε_e is an effective total sky emissivity that, when combined with the air temperature, yields an estimate of the IR flux. For clear-sky conditions, ε_e typically becomes an empirical function of atmospheric water vapor content — either the local humidity, q_a, or the total integrated column water vapor, *IV*. The literature is replete with examples of parameterizations of ε_e as a simple function of local humidity. Josey et al. (2003) offer a variation using T_a and dew point temperature depression, and Garratt (2001) presents another utilizing T_a and *IV* (see Table 3 for units of these variables).

Based on previous studies in the Arctic (Intrieri et al. 2002) and the Subtropics (Fairall et al. 1990; White et al. 1995), we have chosen the Brunt (1932) form for the parameterization of effective emissivity for clear skies, ε_{e0}:

$$\varepsilon_{e0} = A + B\sqrt{q_a} \ . \qquad \textbf{(4)}$$

Using the ETL ship-based radiative flux observations from 15 campaigns (Fairall et al. 2003), we have previously determined the A and B coefficients as simple linear functions of latitude. This fit is based on data obtained between the equator and 60N, but the majority of the data were obtained within 15 degrees of the equator. As we move poleward, the sensitivity to local near-surface water vapor decreases and the constant term increases. For this study, we optimized the fit using only data from the PACS cruises within 15 degrees of the equator. This gives a result:

$$A = 0.50 + \frac{0.13}{60} abs(latitude) \ ; \ B = 0.091 - \frac{0.03}{60} abs(latitude) \, . \qquad \textbf{(5)}$$

We also considered using *IV* for a three-parameter fit. The *IV* is usually obtained by integrating a water vapor profile (e.g., from a sounding) or through retrieval of surface or satellite-based microwave radiance, although values from operational weather forecast models could also be used. Adding the column water vapor gives a fit of the form:

$$\varepsilon_{e0} = A + B\sqrt{q_a} - 0.0188 + 0.0063\,IV\,. \qquad \textbf{(6)}$$

Slight adjustments in the latitude dependences are required to provide a better fit when using column water vapor in this expression. The fits are based on approximately 2300 10-min observations (out of a total of 22,127 observations within 15 degrees of the equator with simultaneous column water vapor measurements). Clear skies were diagnosed by requiring zero cloud fraction from 25-min before to 25-min after the observation time.

Figure 16 shows measurements and two-parameter model values of downward IR flux for periods when the ceilometer-measured cloud fraction is 0 for a continuous 60- min time period. Individual points well above the line are caused by clouds in the field of view of the PIR but are not directly above the ceilometer. Figure 17 shows the residuals between the measured data and the model as a function of the column water vapor. A linear fit of these residuals (with a few small adjustments to *A* and *B*) was used to obtain the three-parameter model. The two-parameter fit has a bias of -1.8 Wm^{-2} and a standard deviation of 7 Wm^{-2}, whereas the three-parameter fit has a bias of -0.9 Wm^{-2} and a standard deviation of 5.7 Wm^{-2}. To reject outliers, we made use of the cumulative probability distribution of the residuals to estimate the standard deviation. The two-parameter fit is biased low by almost 10 Wm^{-2} at the equator, while the three-parameter fit does not show a demonstrable bias.

The uncertainty of the clear-sky models as estimated from the standard deviation for the 10-min observations is surprisingly small, even using the two-parameter fit. This variability must include a contribution from the error in IR measurements, but the relatively small uncertainty is most likely due to a combination of the dominance of MBL water vapor in the downward surface IR flux in the tropics (Stephens and Webster 1981) and the lack of synoptic variability in clear conditions.

As a further demonstration of the utility of the clear-sky concept, we used applied the clear-sky model to TAO buoy data at 95W 5S. Estimates of *IV* were obtained from the ECMWF reanalysis for the years 1999-2002, and surface temperature and specific humidity are obtained from buoy measurements at 3m. Periods of 'clear sky' were selected based on criteria that incoming solar flux exceed 500 W/m^{-2} and the ratio of the modeled solar clear sky flux (see next section) to the observed solar flux exceed 0.94. From the original 202 days of available surface data at this buoy, 4863 ten-minute average clear sky samples meet the criteria. In Figure 18, we present a distribution of the difference between the observed and modeled IR flux from the 95W 5S buoy. Distributed points to the right of 20 Wm^{-2} are most likely an indication of cloudy sky conditions which were not removed from the arbitrary solar flux criteria described above (for example, mid-day clouds which fail to sufficiently block solar flux from the surface instrument). We see that the distribution of points is relatively symmetric and narrow (indicating relatively accurate IR clear sky modeling), with a slightly negative mean value. In fact, the time series of

the difference between the measured IR flux at the surface and the modeled flux (not shown) exhibit an annual structure, with a bias of about +7 Wm^{-2} (model underestimation) in the spring and about -7 Wm^{-2} in mid-summer. This cyclical bias could be attributed to variability in the water vapor or thermal structure in the troposphere which is not captured in the clear sky IR model.

6.2. Solar Flux

Clear-sky parameterizations for solar flux based on specification of atmospheric profiles are available which are similar to the IR flux. Comparable accuracies are more difficult because of the greater effect of aerosols, which vary significantly both seasonally and globally. Unlike the IR flux, which tends to have a relatively isotropic angular distribution, the clear-sky solar flux is highly anisotropic with a peak in the direction of the sun. We are using the solar flux parameterization from Iqbal (1998) which contains components to track the angular position of the sun as a function of day of the year, time of day, and latitude. The solar flux constant at the top of the atmosphere is set to 1367 Wm^{-2}, and the transmission coefficient of the atmosphere is estimated from specifications of total column ozone, aerosol optical thickness in two wave bands, and the column integrated water vapor *IV* as above. We then tune the model by plotting the time series of measured R_{sd}, and comparing it to computed clear-sky values from the algorithm. The aerosol values are then adjusted to fit the peak solar flux for clear days on a cruise-by-cruise basis.

For this approach, it is necessary to specify *IV*. In cases where *IV* is not available, we estimate it from q_a with a ratio relationship $IV = q_a/b$, where b is a coefficient. This ratio is highly dependent on location and season. For example, in subsidence regions the atmosphere above the boundary layer is very dry and b will be large. All PACS cruises have measurements of both *IV* and q_a, which allows us to estimate b. In the eastern tropical Pacific, this constant has a strong latitudinal dependence in fall but a weak dependence in spring (Figure 19), and this structure is most likely a result of synoptic-scale subsidence south of the equator which dries out the upper troposphere and promotes the formation of stratocumulus clouds. We also find that slightly different aerosol coefficients are required in the fall versus the spring. Thus, we have prescribed different aerosol values for spring and fall, but apply the same set to all cruises in a given season.

It is more difficult to assess the accuracy of the shortwave model on short time scales because the vertical cloud fraction gives an imperfect characterization of clouds blocking the sun. We have examined this issue by computing the probability distribution (Figure 20) of the measured-modeled difference in solar flux for cases where the solar zenith angle is less than 20 degrees and cloud fraction is zero (471 samples meet these conditions). The negative tail of the distribution represents cases where the sun is behind an off-zenith cloud. Positive values are due to variations in conditions plus the additional flux contributed from reflecting clouds when the sun is not blocked.

The peak of this distribution occurs at 0 Wm^{-2} (i.e., no model bias), and it has a half-width at half-maximum (an estimate of the standard deviation) of 20 Wm^{-2}. If we establish a threshold by requiring solar flux to exceed 900 Wm^{-2} instead of using solar zenith angle, we

obtain 1200 samples with the peak of the distribution at -10 Wm^{-2} and with approximately the same width. Because some of this width is caused by cloud reflections and random variability in the measurements, we estimate the standard deviation of the model near the solar peak to be 15 Wm^{-2} with a model bias of about -5 Wm^{-2}. In fact, a substantial portion of the true variability is not sampled due to the twice-yearly (spring and fall) schedule for the cruises, and we suspect subsequent aliasing from mesoscale to intraseasonal variability. For *daily average* solar fluxes where measurements of column water vapor are available, these values correspond to a model bias of -2 Wm^{-2} and a standard deviation of 5 Wm^{-2}.

6.3. Implications for Accuracy of SCF

The bias and variability quoted for the clear-sky models are not absolute accuracies, but are computed relative to the data from which they are tuned. We use models for computing SCF in a statistical sense. That is, we are concerned with the mean measured flux minus the mean clear-sky modeled flux. Because we have tuned the model to the data we are analyzing, biases in the measurements will, to first order, cancel in the computation of SCF. For daily average values, the uncertainty in SCF will be about 5–7 Wm^{-2} for both IR and solar fluxes. Note that if these clear-sky models are applied to other datasets without tuning, the uncertainties could be significantly greater, reflecting both the greater uncertainty in the absolute accuracy of the clear-sky models and in the absolute accuracy of the radiative flux measurements.

7. CLOUD FORCING ANALYSIS

In this section we will examine two aspects of SCF in the eastern equatorial Pacific: the seasonality of SCF (similar to the other atmospheric properties presented in section 4) and the mean dependence of SCF on cloud fraction.

The latitudinal dependence of clear-sky net fluxes is shown in Figure 21. The counterintuitive asymmetry about the equator for the clear-sky solar flux is caused by the time of year of the observations (see comment in section 6). The more negative clear-sky net IR flux in the fall is caused by the lower atmospheric water vapor during that season. The slightly stronger latitudinal variation of net IR flux in the fall is associated with stronger variations in atmospheric temperature and water vapor (Figures 5 and 7). The average of the two seasonal curves gives a net solar clear-sky flux of about 300 Wm^{-2} and a net IR clear-sky flux of -68 Wm^{-2} north and -78 Wm^{-2} south of the equator. Based on Earth Radiation Budget Experiment (ERBE) data, Tian and Ramanathan (2002) report annual averages for solar flux in the range 270–275 Wm^{-2} and IR flux of about -60 Wm^{-2} in the north and -80 Wm^{-2} in the south. Our results are not annual averages, so the significance of the similarities is limited without further study.

The mean SCF for both solar and IR is shown in Figure 22. For both SW and LW fluxes, the most obvious seasonal CF difference is the larger magnitudes associated with greater cloudiness in the northern ITCZ. Using the cloud fraction from Figure 11, we have computed the maximum surface cloud forcing (MSCF), and this is illustrated in Figure 23. Here we used the 24-hr cloud fraction for IR flux and the clear-sky solar flux-weighted cloud fraction for solar flux. The 24-hr cloud fraction does not correlate well with daily SW SCF and, in the case of the

mean day-night differences in *f*, may lead to biases in solar MCF. Because the daily average solar flux is relatively sensitive to cloudiness around local noon, we find that the clear-sky solar-weighted cloud fraction provides a better representation than the daytime *f*. For all latitudes, the IR MCF is about 15 Wm^{-2} lower in spring than in fall. The daily values plotted on the CF phase diagram (Figure 24) provide a striking contrast to the typical behavior in most of ETL's tropical cruises. Rather than tending to lie near a single characteristic line, the PACS/EPIC data are scattered from tropical to storm track lines. This clearly indicates that all three principal climate zones (tropical, trade wind, and stratocumulus) are encountered within 10 degrees of the equator in the eastern Pacific. From this figure, we interpret that the spring has a more tropical signature while the fall period is biased toward trade wind and stratocumulus behavior. The deep convective events in the fall often have very strong cold-air downdrafts that lead to sharp reductions in the near surface air temperature which might invalidate the simplistic representation of the IR clear-sky flux.

Of course, cloud forcing depends on cloud fraction. In the simplest case, each cloud's radiative properties are similar to all others, and then CF depends upon the number of clouds in the field. Thus, the radiative flux at the surface can be written

$$R_x = R_{x0} + f * MCF_x = (1 - f)R_{x0} + fR_{x1}. \quad \textbf{(7)}$$

This approach forms the basis for simple treatments of fractional cloudiness (Hartmann et al. 1992). For solar flux, nonlinear dependencies on vertical *f* are common (Katsaros 1990; Grant and Hignett 1998). In addition, hemispherically-averaged cloud fraction or cloud fraction at the solar zenith angle (White et al. 1996) have also been used. Thus, a linear dependence of CF on cloud fraction implies that such simple models are applicable. Here, we illustrate this dependence using the daily-averaged solar and IR fluxes with a 24-hr averaged (for IR) or daytime averaged (for solar) cloud fraction (Figure 25). For IR flux, a linear regression gives $MCF_l = 50$ Wm^{-2}. However, a 2^{nd}-order fit gives a linear term of 33 Wm^{-2} and a quadratic coefficient of 20 Wm^{-2}. Thus, for low cloud fractions IR MCF is less than for high cloud fractions (i.e., 33 vs. 53 Wm^{-2}). For solar flux, the data are too scattered to determine nonlinearity, but a linear regression results in $MCF_s = -135$ Wm^{-2}.

Figure 26 shows the results of averaging the daily values into bins of cloud fraction where we separate spring (74 days) and fall (86 days) cruises. This figure clearly shows lower LW CF in the spring than in the fall. For cloud fraction less than 0.5, the fall SW CF values are smaller in magnitude, but slightly larger for high cloud fractions (greater than 0.7). This is qualitatively consistent with the lower cloudy liquid water path values found south of 3N and the larger values north of 6N in fall versus spring (see the discussion at the end of section 5). Therefore, for solar SCF there are some small seasonal differences that are not attributable to cloud fraction but are probably associated with the actual liquid water content of the clouds. Linear regressions to these data imply IR MCF of 53 Wm^{-2} in fall and 40 Wm^{-2} in spring, with solar MCF values of -141 Wm^{-2} in fall and -127 Wm^{-2} in the spring. Averaging in this form has removed much of the apparent nonlinearity from Figure 25, suggesting that it was partly caused by mixing spring and fall data.

8. CONCLUSIONS

We analyzed air-sea flux and cloud measurements from a series of seven cruises made in the eastern equatorial Pacific between fall 1999 and fall 2002. The cruise location includes the equatorial cold tongue and the ITCZ, and the measurements are coincident with the enhanced TAO buoy lines along 95W and 110W longitudes. Our analysis has emphasized the statistical properties (mean, variance, probability distribution functions) as a function of latitude contrasting the Northern Hemisphere fall and spring seasons. Of course, seven cruises do not constitute a comprehensive climatology, but many of the mean variables show consistent structures. For most quantities, the variability from year to year during the same season and at the same latitude is quite small (see Table 3), and, with a few exceptions, there was little difference between the two seasons.

The most obvious seasonal differences are the stronger Northern Hemisphere ITCZ and stronger north-south SST difference in the fall periods. We also see much stronger turbulent heat fluxes in the SST frontal region north of the equator in the fall. These stronger fluxes drive the rapid MBL adjustment to the changing SST associated with the cross-equatorial air flow. Thus, the colder water south of the equator in fall exerts a strong cooling influence on the ocean north of the equator (an additional 60 Wm^{-2} compared to spring). The strong ITCZ region north of the equator in the fall also produces much more cloudiness, precipitation, southerly winds, and solar cloud forcing in the region around 6N.

We examined cloud fraction, cloud base height statistics, and cloudy liquid water path. The fall period was much cloudier north of the equator, with mean cloud fraction about 90% at 6N. The spring clouds showed a strong diurnal variation with substantially lower cloud fraction during the day south of 5N (except in the southern ITCZ region at 4S). This may be a result of greater subsidence or surface heating during the day. Simple averages of cloud base heights were presented, and, by looking at the peak in the distribution (i.e., the most probable cloud base height), we demonstrated the significant effects on clouds near the equator. The lower cloud bases there reflect the surface stability transition and episodic decoupling of the MBL as air from the south encounters the equatorial cold tongue. The equatorial effects were more dramatic in the fall when the cold tongue is much colder. At the equator, very low clouds were occasionally observed with a fairly even distribution of cloud bases.

Surface cloud radiative forcing is defined as the difference in mean observed net radiative flux and that flux which would be observed in the absence of clouds. To investigate this, we first estimated the clear-sky radiative fluxes, and we employed two simple models requiring near-surface temperature, humidity, and estimates of column water vapor and aerosol optical depth. The model parameters were tuned for a best fit to the radiative fluxes observed during clear periods. By turning the models to the data, we are able to produce estimates of CF within 5–7 Wm^{-2} for daily-averaged radiative fluxes. The models are intended to be applicable for buoys and ships where column water vapor measurements are not available, although regional accuracy will be compromised without specific tuning.

For IR fluxes, CF strongly correlates with cloud fraction. There are substantial seasonal differences in IR CF but relatively modest seasonal differences in MCF (53 Wm^{-2} in the fall versus 40 Wm^{-2} in spring). For solar fluxes, MCF is about -135 Wm^{-2}; MCF_s is stronger in the

spring between 3S and 6N with values around -250 Wm^{-2} at and just south of the equator (Figure 23). However, these unusual spring values are actually realized in regions with low daytime cloud fraction, so the significance is uncertain. When averaged in cloud fraction bins, the fall versus spring differences are fairly small (Figure 26). There is some evidence for lower liquid water leading to lower solar MCF for broken clouds in the fall, but these differences are near the sampling resolution of the averages. The ratio of solar to IR MCF (-135/53 = -2.5) implies that clouds in this region strongly cool the surface. However, the IR CF is significantly greater than the observations for a typical ETL tropical cruise (see Figure 15), so the net cooling effect is less than that of the tropical western Pacific.

Finally, the contributions of clouds to the net surface heat budget are shown in Figure 27. The net heat flux (upper panel) shows a striking symmetry difference between the spring and fall. The spring net heat flux is nearly symmetrical about the equator with a maximum (175 Wm^{-2}) at the equator decreasing to about 100 Wm^{-2} at 10N and 8S. The equatorial maximum is associated with lower turbulent fluxes and modestly lower cloudiness at the equator. In the fall, the maximum net heat flux (180 Wm^{-2}) is at 2S and the minimum (essentially 0) is at 6N. There is also a significant asymmetry away from the equator (125 Wm^{-2} at 8S versus 75 Wm^{-2} at 10N). Clearly, the minimum CF at 6N is primarily associated with strong solar CF (lower panel in Figure 27) associated with the ITCZ. The maximum just south of the equator is associated with much weak turbulent cooling (Figure 8) and weak solar CF. Solar CF is also much more equatorially asymmetric in the fall (Figure 27).

Our results offer considerable characterization of the statistical properties of the MBL and surface forcing of the eastern equatorial Pacific ITCZ/Cold Tongue complex twice a year at times near the maximum seasonal contrast. We have attempted to not only characterize the variability but also to isolate the role of cloud radiative forcing in that variability, and this includes providing information on cloud properties. Because our measurements do not include a strong El Niño event, this study cannot be considered a complete characterization of the statistics, but does provide significant detail to establish basic characterization for non-El Niño conditions. Soundings from these cruises have already formed the basis of a study of parameterizations of MBL depth in climate models (Zeng et al. 2004). A much more complete investigation of the annual cycle and inter-annual variability is underway using data from the TAO buoys in this region (Cronin et al. 2002). In addition, an analysis of C-band radar characterizations of deep convection is presently under way. In 2003, we inaugurated a related study during an annual fall cruise to the WHOI *Stratus* buoy at 20S 95W (http://uop.whoi.edu/stratus/). This buoy is located in the heart of the South Pacific stratocumulus belt off South America (Hartmann et al. 1992).

Acknowledgments. This work was supported by the NOAA Office of Global Programs, ONR Marine Meteorology program, the DOE Atmospheric Radiation Measurement program, and the National Science Foundation Climate Dynamics program. The authors especially thank Scott Abbott, Dave Costa, Mike Falls, Dan Gottas, Jim Jordan, Jesse Leach, Brenda Mulac, Jeff Otten, Bill Otto, Sergio Pezoa, Michelle Ratterree, Cat Russell, Kara Sterling, and Dan Wolfe for work, dedication, and personal sacrifice in doing the field work. The contributions and help of the crews of the NOAA ships *Ronald H. Brown* and *Ka'imimoana* is greatly appreciated.

9. REFERENCES

Albrecht, B.A., 1989: Aerosols, cloud microphysics, and fractional cloudiness. *Science*, **245**, 1227–1230.

————————, 1993: The effects of drizzle on the thermodynamic structure of the trade wind boundary layer. *J. Geophys. Res*., **98**, 7327–7337.

Berg, L.K. and R.B. Stull, 2002: Accuracy of point and line measures of boundary layer cloud amount. *J. Appl. Meteor.*, **41**, 640–650.

Bond, N.A., 1992: Observations of planetary boundary-layer structure in the eastern equatorial Pacific. *J. Climate,* **5**, 699–706.

Bretherton, C.S., T. Uttal, C.W. Fairall, S.E. Yuter, R.A. Weller, D. Baumgardner, K. Comstock, and R. Wood, 2004: The EPIC 2001 Stratocumulus Study. *Bull. Amer. Meteor. Soc*., to appear.

Browning, K.A., 1994: Survey of perceived priority issues in the parameterizations of cloud-related processes in GCMs. *Quart. J. Roy. Meteor. Soc.*, **129**, 483–487.

Brunt, D., 1932: Notes on radiation in the atmosphere. *Quart. J. Roy. Meteor. Soc*., **58**, 389–420.

Cess, R.D., M.H. Zhang, P. Minnis, L. Corsetti, E.G. Dutton, B.W. Forgan, D.P. Garber, W.L. Gates, J.J. Hack, E.F. Harrison, X. Jing, J.T. Kiehl, C.N. Long, J.-J. Morecrette, G.L. Potter, V. Ramanathan, B. Subasilar, C.H. Whitlock, D.F. Young, and Y. Zhou, 1995: Absorption of solar radiation by clouds: Observations versus models. *Science*, **267**, 496–499.

Collins, W.D., J. Wang, J.T. Keihl, G.J. Zhang, D.I. Cooper, and W.E. Echinger, 1997: Comparisons of tropical ocean-atmosphere fluxes with the NCAR community model CCM3. *J. Climate*, **10**, 3047–3058.

Cronin, M.F., N. Bond, C.W. Fairall, J.E. Hare, M.J. McPhaden, and R.A. Weller, 2002: Enhanced oceanic and atmospheric monitoring for the Eastern Pacific Investigation of Climate Processes (EPIC) experiment. *EOS, Trans. AGU*, **83**, 205–211.

Curry, J. A., and 21 coauthors, 2004: Project SEAFLUX. *Bull. Amer. Meteor. Soc.*, **85**, 409–424.

Delecluse, P., M.K. Davey, Y. Kitamura, S.G.H. Philander, M. Suarez, and L. Bengtsson, 1998: Coupled general circulation modeling of the tropical Pacific. *J. Geophys. Res*., **103**, 14 357–14 373.

Ecklund, W.L., D.A. Carter, and B.B. Balsley, 1988: An UHF profiler for the boundary layer: Brief description and initial results. *J. Atmos. Ocean. Technol*., **5**, 432–441.

———————, P.E. Johnston, J.M. Warnock, W.L. Clark, and K.S. Gage, 1999: A 3-GHz profiler for precipitating cloud studies. *J. Atmos. Ocean. Technol.*, **16**, 309–322.

Edson, J.B., A.A. Hinton, K.E. Prada, J.E. Hare, and C.W. Fairall, 1998: Direct covariance flux estimates from moving platforms at sea. *J. Atmos. Ocean. Technol.,* **15**, 547–562.

Esbensen, S., T. Mitchell, and C. Gudmundson, 2002: U. S. CLIVAR Pan American Research: A scientific prospectus and implementation plan. U.S. CLIVAR OFFICE, Washington, D.C., 58 pp.

Fairall, C.W., J.E. Hare, and J.B. Snider, 1990: An eight-month sample of marine stratocumulus cloud fraction, albedo, and integrated liquid water. *J. Climate*, **3**, 847–864.

———————, E.F. Bradley, J.S. Godfrey, G.A. Wick, J.B. Edson, and G.S. Young, 1996a: Cool-skin and warm-layer effects on sea surface temperature. *J. Geophys. Res.*, **101**, 1295–1308.

———————, ———————, D.P. Rogers, J.B. Edson, and G.S. Young, 1996b: Bulk parameterization of air-sea fluxes for Tropical Ocean - Global Atmosphere Coupled-Ocean Atmosphere Response Experiment. *J. Geophys. Res.*, **101**, 3747–3764.

———————, J.B. Edson, and J.E. Hare, 1997: Integrated shipboard measurements of the marine boundary layer. *J. Atmos. Oceanic Tech.*, **14**,338–359.

———————, O.P.G. Persson, R.E. Payne, and E.F. Bradley, 1998: A new look at calibration and use of Eppley precision infrared radiometers. *J. Atmos. Ocean. Technol.*, **15**, 1230–1243.

———————, E.F. Bradley, J.E. Hare, A.A. Grachev, and J.B. Edson, 2003: Bulk parameterization of air-sea fluxes: Updates and verification for the COARE algorithm. *J. Climate*, **16**, 571–591.

Frisch, A.S., C.W. Fairall, and J.B. Snider, 1995: On the measurement of stratus cloud and drizzle parameters with a K_α-band Doppler radar and a microwave radiometer. *J. Atmos. Sci.,* **52**, 2788–2799.

———————, G. Feingold, C.W. Fairall, T. Uttal, and J.B. Snider, 1998: On cloud radar and microwave radiometer measurements of stratus cloud liquid water profiles. *J. Geophys. Res*., **103**, 23195–23197.

———————, M. Shupe, I. Djalalova, G. Feingold, and M. Poellot, 2002: The retrieval of stratus cloud droplet effective radius with cloud radars. *J. Atmos. Ocean. Technol*., **19**, 835–842.

Garratt, J.R., 2001: Clear-sky longwave irradiance at the Earth's surface - Evaluation of climate models. *J. Climate*, **14**, 1647–1670.

——————— and A.J. Prata, 1996: Downwelling longwave fluxes at continental surfaces - A comparison of observations with GCM simulations and implications for the Global Land-Surface Radiation Budget. *J. Climate*, **9**, 646–655.

Grant, A.L.M., and P. Hignett, 1998: Aircraft observations of the surface energy balance in TOGA-COARE. *Quart. J. Roy. Meteor. Soc*., **124**, 101–122.

Hartmann, D.L., M.E. Ockert-Bell, and M.L. Michelsen, 1992: The effect of cloud type on Earth's energy balance: Global analysis. *J. Climate*, **5**, 1281–1304.

Hashizume, H., S.-P. Xie, M. Fuijiwara, M. Shiotani, T. Watanabe, Y. Tanimoto, W.T. Liu, and K. Takeuchi, 2003. Direct observations of atmospheric boundary layer response to SST variations associated with tropical instability waves over the Eastern Equatorial Pacific. *J. Climate*, **15**, 3379–3393.

Intrieri, J. M. C. W. Fairall, M. D. Shupe, P. O. G. Persson, E. L. Andreas, P. S. Guest, and R. E. Moritz, 2002: Annual cycle of cloud forcing at SHEBA. *J. Geophys. Res.*, **107**, NO. C10, 8039, doi:10.1029/2000JC000439, 2002.

Iqbal, M., 1998: Spectral and total sun radiance under cloudless skies. *Physical Climatology for Solar and Wind Energy*, R. Guzzi and C. G. Justus, Eds., World Scientific, 196–242.

Jones, C., P. Peterson, C. Gautier, and W.T. Liu, 2001: Satellite observations of latent and sensible heat fluxes in the tropical Pacific Ocean. *Proc. WCRP/SCOR Workshop on Intercomparison and Validation of Ocean-Atmosphere Flux Fields.* Potomac, MD, 21-24 May, WCRP Report #115, 209–214.

Josey, S.A., E.C. Kent, and P.K. Taylor, 2002: Wind stress forcing of the ocean in the SOC climatology: Comparisons with the NCEP-NCAR, ECMWF, UWM/COADS, and Hellerman and Rosenstein datasets. *J. Phys. Oceanogr.*, **32**, 1993–2019.

———————, P.W. Pascal, P.K. Taylor, and M.J. Yelland, 2003: A new formula for determining the atmospheric longwave flux at the ocean surface at mid-high latitudes. *J. Geophys. Res.*, **108**, 3108, doi:10.1029/2002JC001418, 5–1 to 5–16.

Katsaros, K.B., 1990: Parameterization schemes and models for estimating the surface radiation budget. *Surface Waves and Fluxes, Vol. II.* G.L. Geernaert and W.J. Plant, Eds., Kluwer Academic Publishers, 339–368.

Key, J.R., R.A. Silcox, and R.S. Stone, 1996: Evaluation of surface flux radiative flux parameterizations for use in sea ice models. *J. Geophys. Res.,* **101***,* 3839–3849.

Li, T. and S.G.H. Philander, 1996: On the annual cycle of the eastern equatorial Pacific. *J. Climate*, **9**, 2986–2998.

Liljegren, J.C., E.E. Clothiaux, G.G. Mace, S. Kato, and X. Dong, 2001: A new retrieval for cloud liquid water path using a ground-based microwave radiometer and measurements of cloud temperature. *J. Geophys. Res.*, **106**, 14 485–14 500.

Lind, R.J. and K.B. Katsaros, 1984: Radiation budget components and their parameterization in JASIN. *Quart. J. Roy. Meteor. Soc.*, **110**, 1061–1071.

Matrosov, S., A. Heymsfield, J. Intrieri, B. Orr, and J.B. Snider, 1995: Ground-based remote sensing of cloud particles sized during the November 26, 1991 FIRE II cirrus case. *J. Atmos. Sci*., **52**, 4128–4142.

McPhaden, M.J. and coauthors, 1998: The Tropical Ocean Global Atmosphere observing system: A decade of progress. *J. Geophys. Res*., **103**, 14 169–14 240.

Menon, S., A.D. DelGenio, D. Koch, and G. Tselioudis, 2002: GCM simulations of the aerosol indirect effect: Sensitivity to cloud parameterization and aerosol burden. *J. Atmos. Sci.*, **59**, 692–713.

Miller, M.J., A.C.M. Beljaars, and T.N. Palmer, 1992: The sensitivity of the ECMWF model to the parameterization of evaporation from the tropical oceans. *J. Climate*, **5**, 418–434.

Miller, M. A., M. J. Bartholomew, and R. M. Reynolds, 2004: The accuracy of marine shadow-band sun photometer measurements of aerosol optical thickness and Angstrom exponent. *J. Atmos. Ocean. Techno*., **21**, 397-410.

Mlawer, E.J., S.J., Taubman, P.D. Brown, M.J. Iacono, and S.A. Clough, 1997: Radiative transfer for inhomogeneous atmospheres: RRTM, a validated correlated-k model for the longwave. *J. Geophys. Res.*, **102**, 16 663–16 682.

————————, P.D. Brown, S.A. Clough, L.C. Harrison, J.J. Michalsky, P.W. Kiedron, and T. Shippert, 2000: Comparison of spectral direct and diffused solar irradiance measurements and calculations for cloud-free conditions. *Geophys. Res. Lett*., **27**, 2653–2656.

Moran, K.P., B.E. Martner, M.J. Post, R.A. Kropfli, D.C. Welsh, and K.B. Widener, 1998: An unattended cloud-profiling radar for use in climate research. *Bull. Amer. Meteor. Soc*., **79**, 443–455.

Norris, J.R. and C.B. Leovy, 1994: Interannual variability in stratiform cloudiness and sea surface temperature. *J. Climate*, **7**, 1915–1925.

Petersen, W.A., R. Cifelli, D.J. Bocippio, S.A. Rutledge, and C.W. Fairall, 2002: Convection and easterly wave structure observed in the Eastern Pacific warm-pool during EPIC-2001. *J. Atmos. Sci.*, **60**, 1754–1773.

Philander, S.G.H., D. Gu, D. Halpern, G. Lambert, N.-C. Lau, T. Li, and R.C. Pacanowski 1996:

Why the ITCZ is mostly north of the equator. *J. Climate*, **9**, 2958–2972.

Pincus, R., M.B. Baker, and C.S. Bretherton, 1997: What controls stratocumulus radiative properties? Lagrangian observations of cloud evolution. *J. Atmos. Sci.*, **54**, 2215–2236.

Ramanathan, V., R.D. Cess, E.F. Harrison, P. Minnis, B.R. Barkstrom, E. Ahmad, and D. Hartman, 1989: Cloud-radiative forcing and climate: Results for the Earth Radiation Budget Experiment. *Science*, **243**, 57–63.

————————, B. Subasilar, G.J. Zhang, W. Conant, R.D. Cess, J.T. Kiehl, H. Grassl, and L. Shi, 1995: Warm pool heat budget nd shortwave cloud forcing: A missing physics? *Science*, **267**, 499–503.

Randall, D.A., J.A. Coakley, C.W. Fairall, R.A. Kropfli, and D.H. Lenschow, 1984: Outlook for research on subtropical marine stratiform clouds. *Bull. Amer. Meteor. Soc*., **64**, 1290–1301.

Raymond, D., J. Esbensen, M. Gregg, and N. Shay, 1999: EPIC2001: Overview and implementation plan. See ftp://kestrel.nmt.edu/pub/raymond/epic2001/overview.pdf.

————————, S.K. Esbensen, M. Gregg, C.S. Bretherton, L.K. Shay, T. Uttal, and P. Zuidema, 2004: EPIC2001 and the coupled ocean-atmosphere system of the tropical East Pacific. *Bull. Amer. Meteor. Soc.*, **85**, 1342-1354.

Smith, S.R., D.M. Legler, and K.V. Verzone, 2001: Quantifying uncertainties in NCEP reanalyses using high-quality research vessel observations. *J. Climate*, **14**, 4062–4072.

Snider, J.B. and D.A. Hazen, 1998: Surface-based radiometric observations of water vapor and cloud liquid water in the temperature zone and in the tropics. *Radio Sci.,* **33**, 421–432.

Stephens, G.L. and P.J. Webster, 1981: Clouds and climate: Sensitivity of simple systems. *J. Atmos. Sci.,* **38**, 235–247.

Stevens, B., J. Duan, J.C. McWilliams, M. Munnich, and J.D. Neelin, 2001: Entrainment, Rayleigh friction, and boundary layer winds over the tropical Pacific. *J. Climate*, **15**, 30-44.

Taylor, P.K., 2001: Intercomparison and validation of ocean-atmosphere flux fields. *Proc. WCRP/SCOR Workshop on Intercomparison and Validation of Ocean-Atmosphere Flux Fields.* Potomac, MD, 21-24 May, WCRP Report #115, 1–4.

Tian, B. and V. Ramanathan, 2002: Role of tropical clouds in surface and atmospheric energy budget. *J. Climate*, **59**, 296–305.

Walsh, J.E. and W.L. Chapman, 1998: Arctic cloud-radiation-temperature associations in observational data and atmospheric reanalyses, *J. Climate*, **11**, 3030–3044.

Webster, P. J. and R. Lukas, 1992: TOGA COARE: The coupled ocean atmosphere response experiment. *Bull. Amer. Meteor. Soc.*, **73**, 1377–1416.

Weller, R., B. Albrecht, S. Esbensen, C. Eriksen, A. Kumar, R. Mechoso, D. Raymond, D. Rogers, and D. Rudnick, 1998: A science and implementation plan for EPIC: An eastern Pacific investigation of climate processes in the coupled ocean-atmosphere system. See http:://www.atmos.washington.edu/gcf/EPIC/.

Weng, F., N. C. Grody, R. Ferraro, A. Basist, D. Forsyth, 1997: Cloud liquid water climatology from the special sensor microwave/imager. *J. Clim.*, **10**, 1086-1098.

Westwater, E.R., B.B. Stankov, D. Cimini, Y. Han, J.A. Shaw, B.M. Lesht, and C.N. Long, 2003: Radiosonde humidity soundings and microwave radiometers during Nauru99. *J. Atmos. Oceanic Technol.*, **20**, 953–971.

White, A.B., C.W. Fairall, and J.B. Snider, 1995: Surface-based remote sensing of marine boundary-layer cloud properties. *J. Atmos. Sci*., **52**, 2827–2838.

————, ————, A.S. Frisch, B.W. Orr, and J.B. Snider, 1996: Recent radar measurements of turbulence and microphysical properties in clouds. *Atmos. Res*., **90**, 117–121.

Wild, M., A. Ohmura, H. Gilgen, and E. Roeckner, 1995: Validation of General Circulation Model radiative fluxes using surface observations. *J. Climate*, **8**, 1309–1324.

Yelland, M.J., B.I. Moat, P.K. Taylor, R.W. Pascal, J. Hutchings, and V.C. Cornell, 1998: Wind stress measurements from the open ocean corrected for airflow distortion by the ship. *J. Phys. Oceanogr.*, **28**, 1511–1526.

Yuter, S.E. and R.A. Houze, 2000: The 1997 Pan American Climate Studies Tropical Eastern Pacific Process Study. Part I: ITCZ region**.** *Bull. Amer. Meteor. Soc.* **81**, 451–482.

———— and W.S. Parker, 2001: Rainfall measurement on ship revisited: The 1997 PACS TEPPS cruise. *J. Appl. Meteorol.*, **40**, 1003–1018.

Zeng, X., M.A. Brunke, M. Zhou, C.W. Fairall, N.A. Bond, and D.H. Lenschow, 2004: Marine atmospheric boundary layer height over the Eastern Pacific: Data analysis and model evaluation. *J. Climate*, to appear.

Zhu, P. and B. Albrecht, 2002: A theoretical and observational analysis of the formation of fair-weather cumuli. *J. Atmos. Sci*., **59**, 1982–2005.

FIGURES

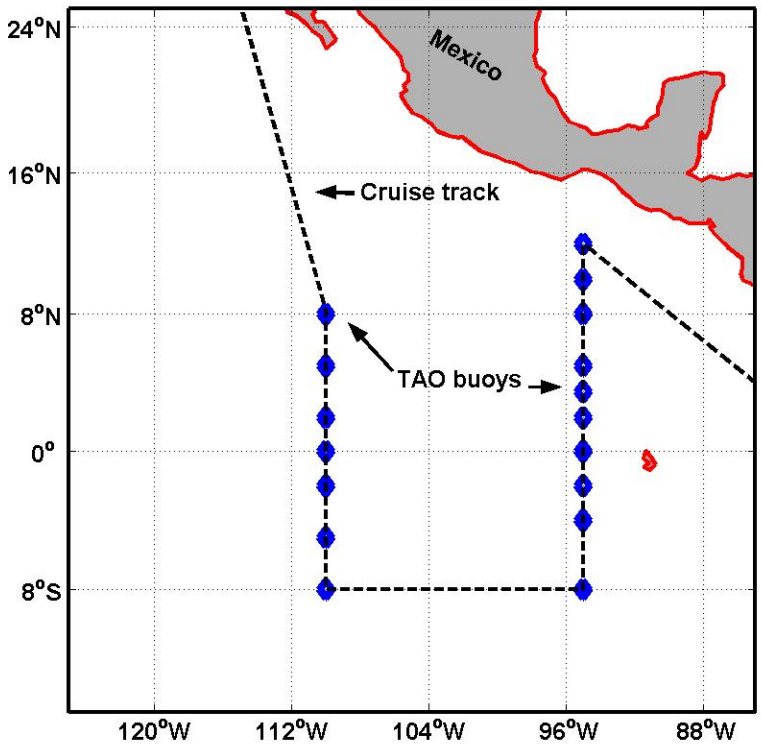

Figure 1. Cruise track for the NOAA Ship *Ronald H. Brown* for the fall 1999 EPIC cruise. Diamonds indicate the locations of TAO buoys. At the conclusion of the cruise, the ship returned to San Diego (not shown).

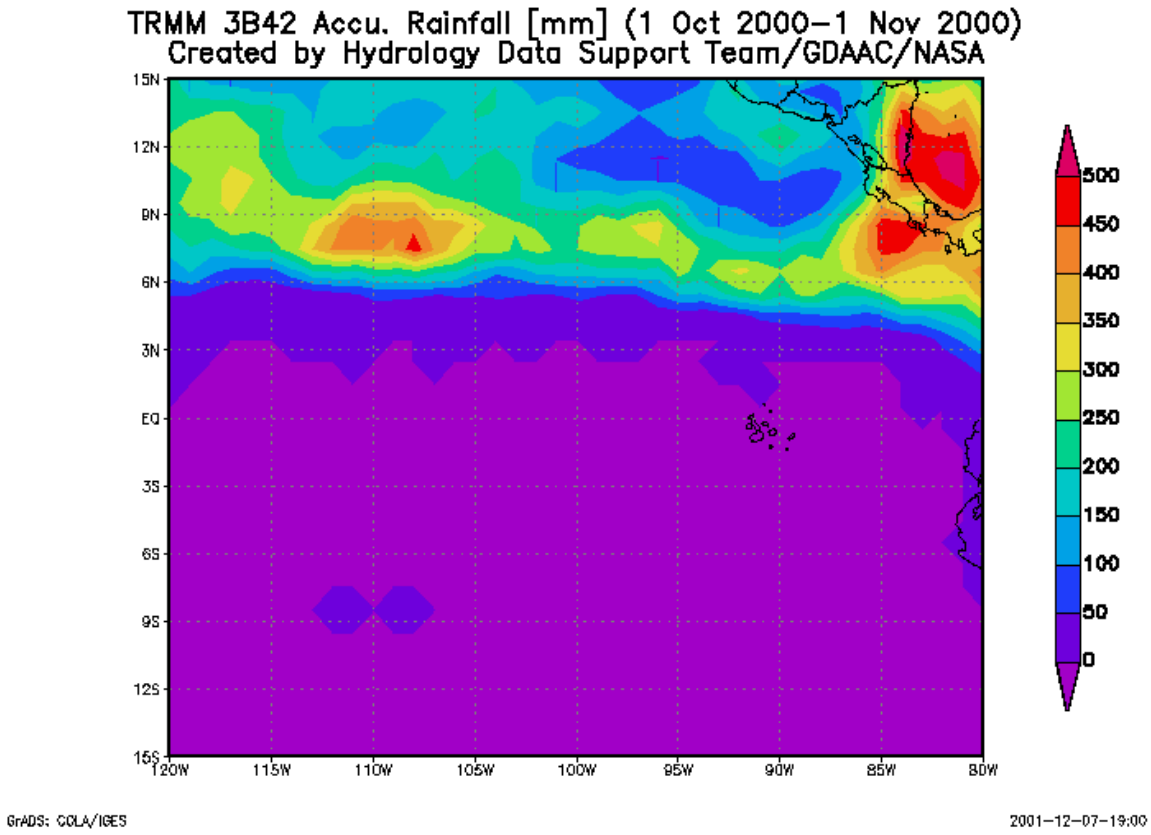

(2a)

Figure 2. One-month rainfall accumulations from the TRMM 3B42 rainfall product for spring (a) and fall (b) 2000 cruises.

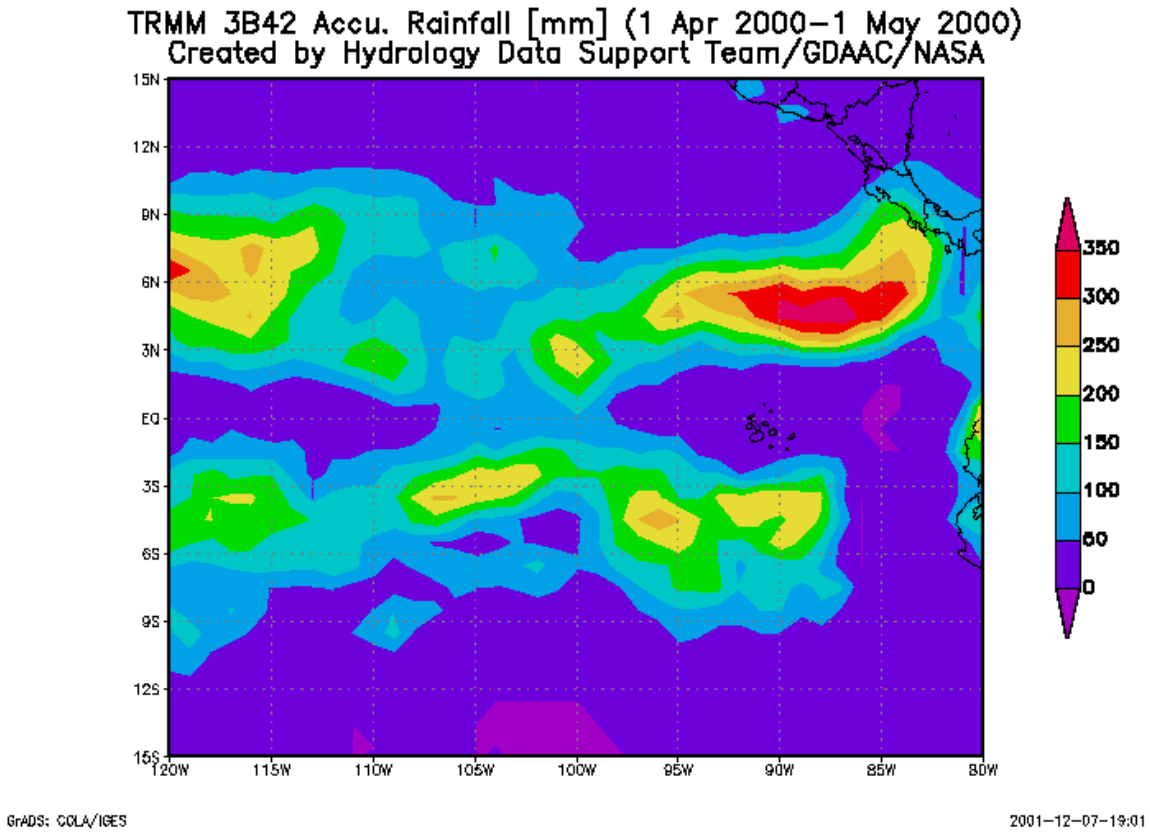
TRMM 3B42 Accu. Rainfall [mm] (1 Apr 2000–1 May 2000)
Created by Hydrology Data Support Team/GDAAC/NASA
15N
12N
9N
6N
3N
EQ
3S
6S
9S
12S
15S
120W
115W
110W
105W
100W
95W
90W
85W
80W
350
300
250
200
150
100
50
0
GrADS: COLA/IGES
2001-12-07-19:01

(2b)

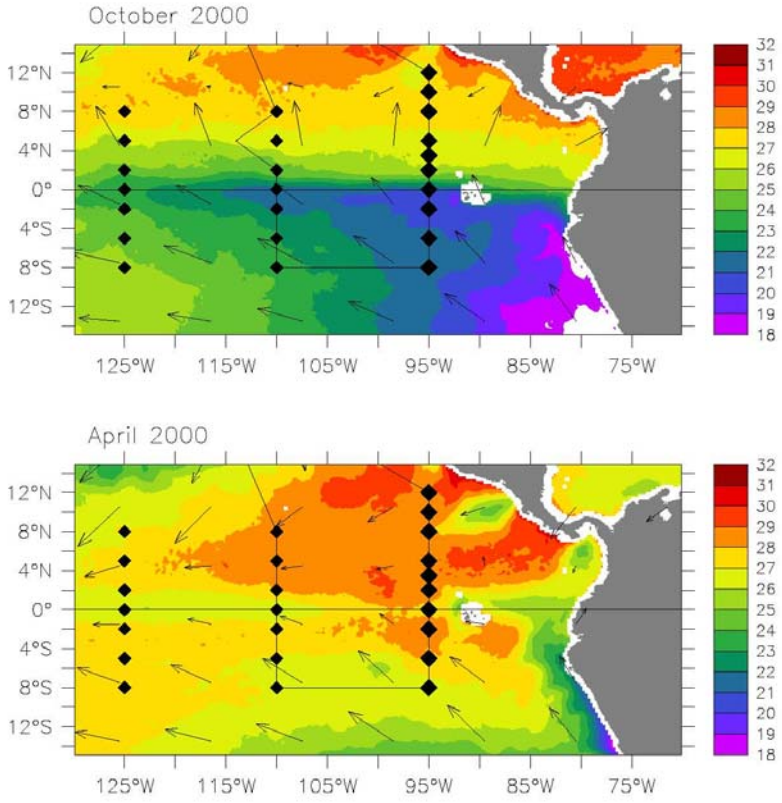

Figure 3. The EPIC mooring array is shown in relation to the September 1998 composite SST and ECMWF wind fields.

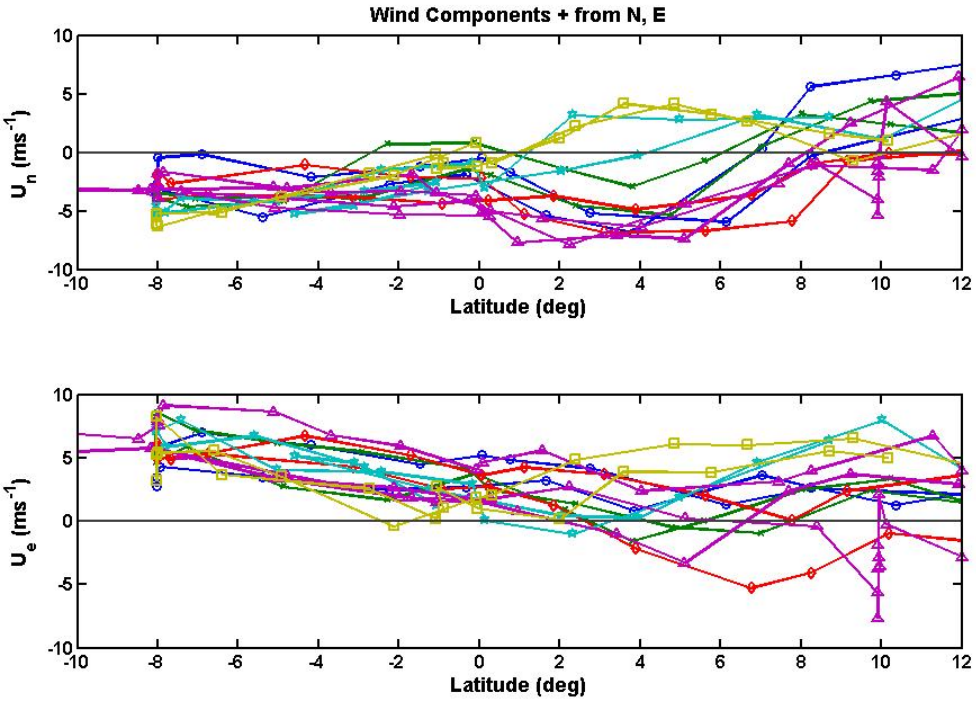

(4a)

Figure 4. Wind components (northerly — upper panel; easterly — lower panel) from seven EPIC cruises. (a) Daily-averaged values, with each symbol representing a single cruise and includes both 110W and 95W longitudinal portions. (b) Latitude average values. Circle — fall; diamond — spring.

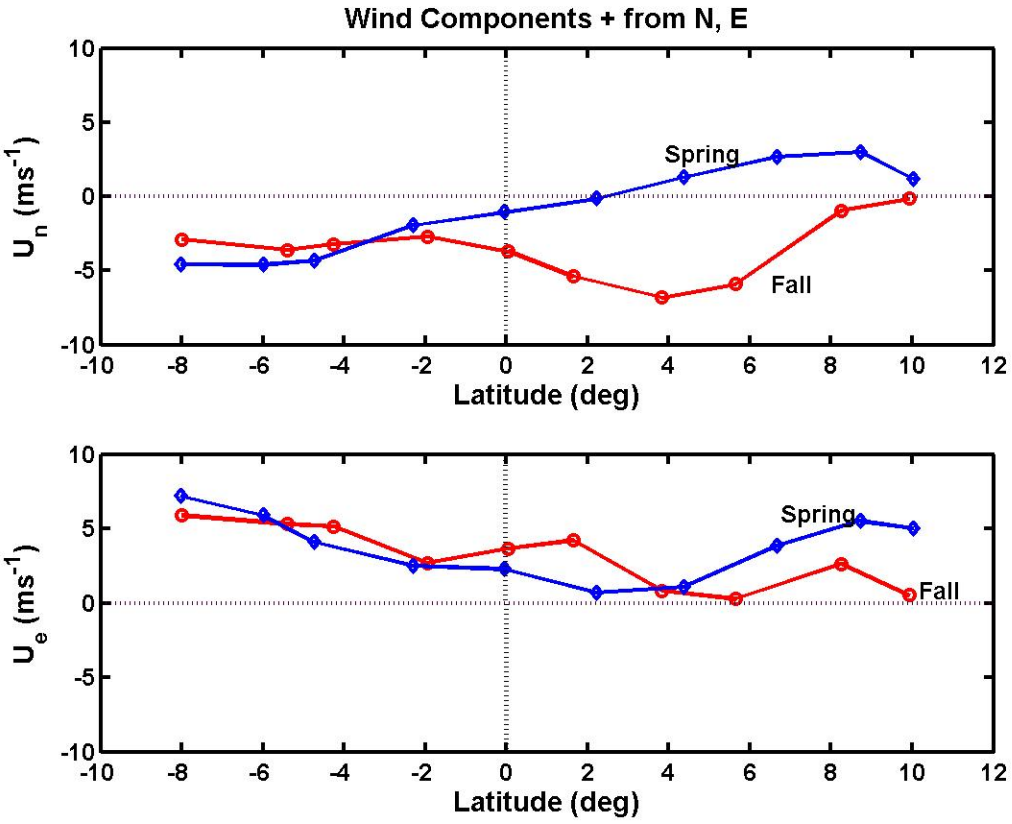
Wind Components + from N, E
U_n (ms^{-1})
Spring
Fall
Latitude (deg)
U_e (ms^{-1})
Spring
Fall
Latitude (deg)

(4b)

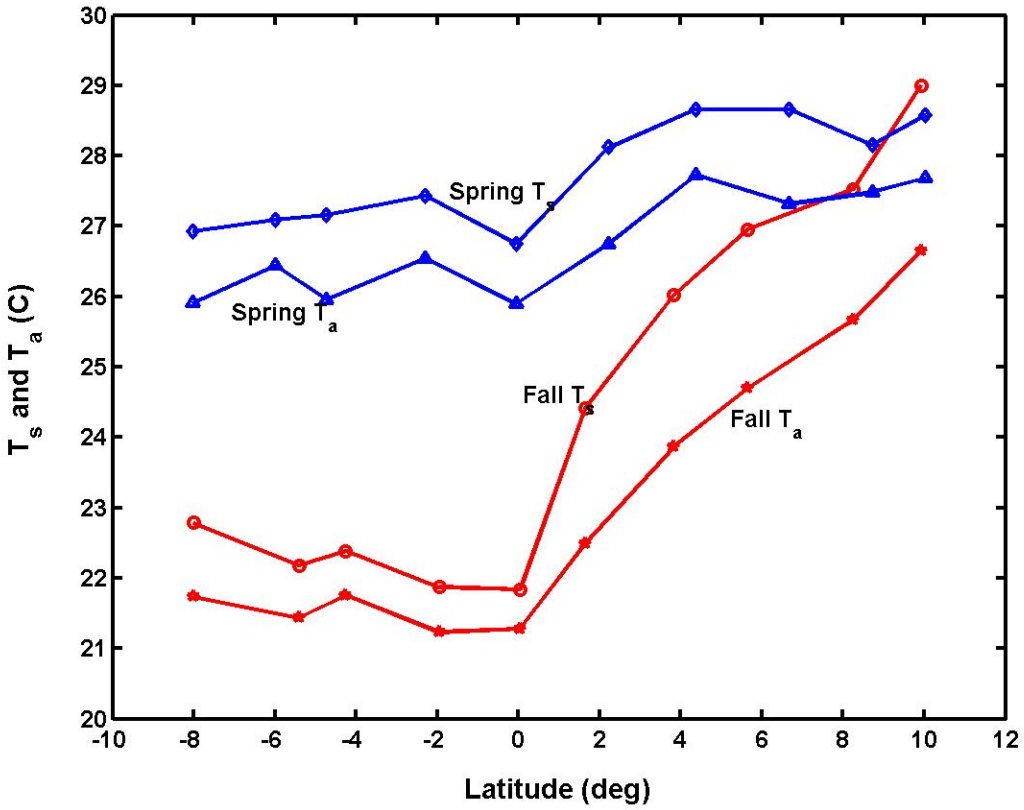

Figure 5. Latitude-averaged temperatures. Circle — fall SST; star — fall T_a; diamond — spring SST; triangle — spring T_a.

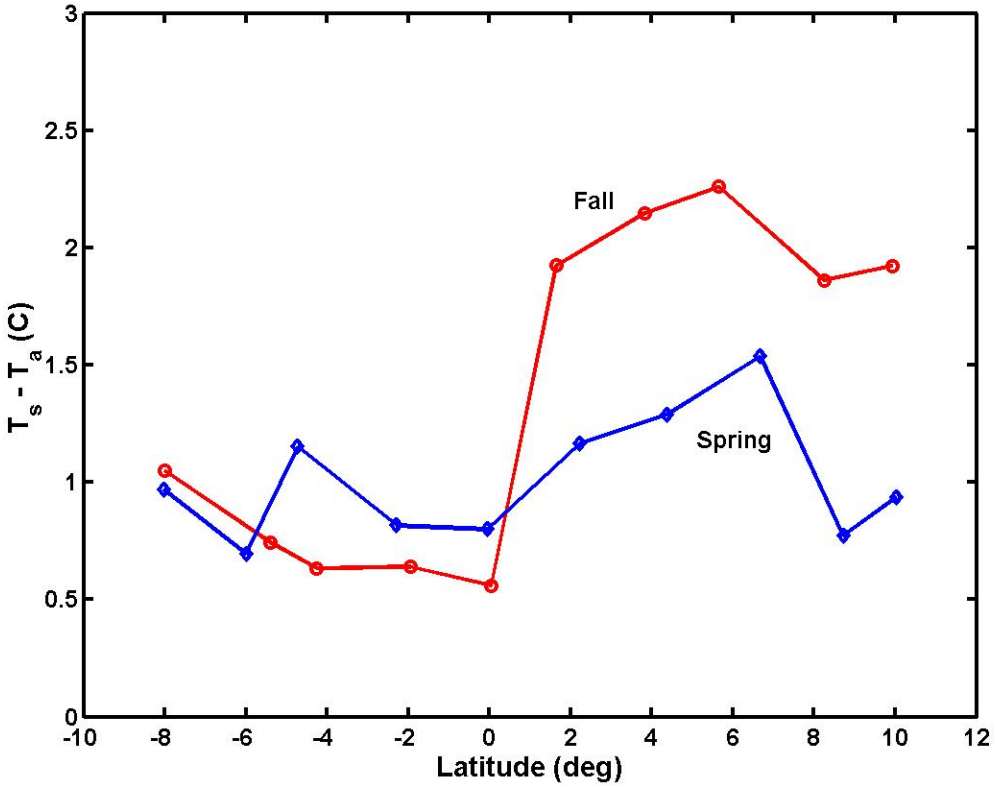

Figure 6. Latitude-averaged sea-air temperature difference. Circles — fall; diamonds — spring.

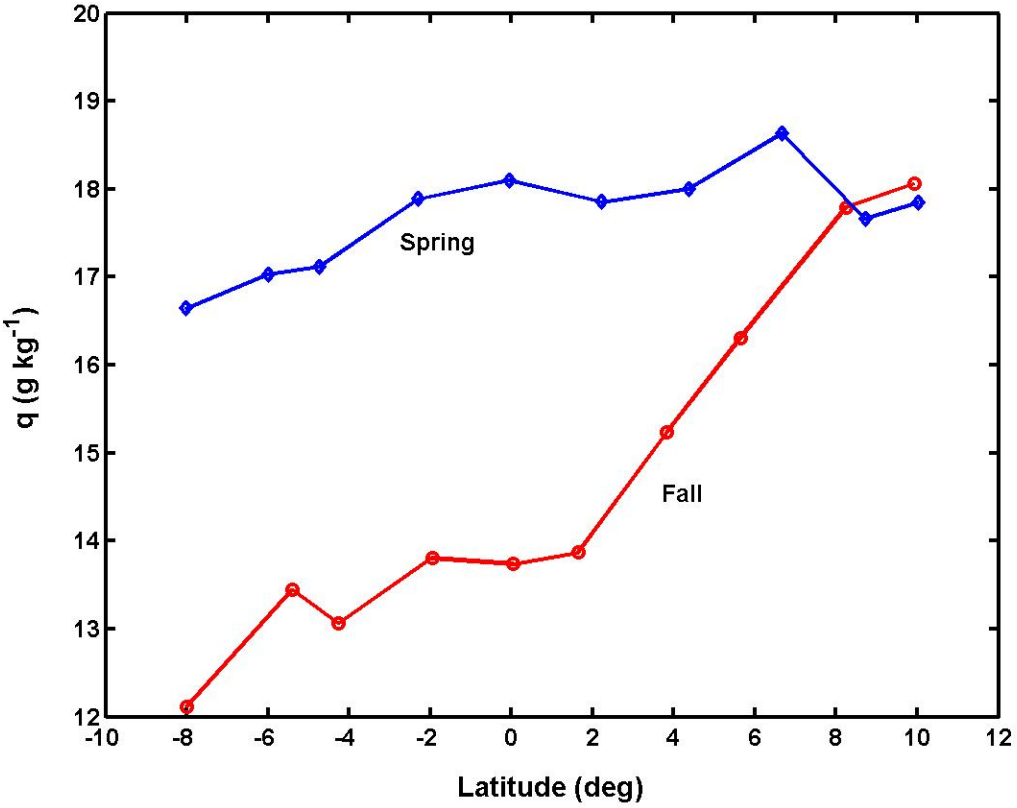

(7a)

Figure 7. Latitude-averaged (a) specific humidity and (b) column integrated water vapor. Circles — fall; diamonds — spring.

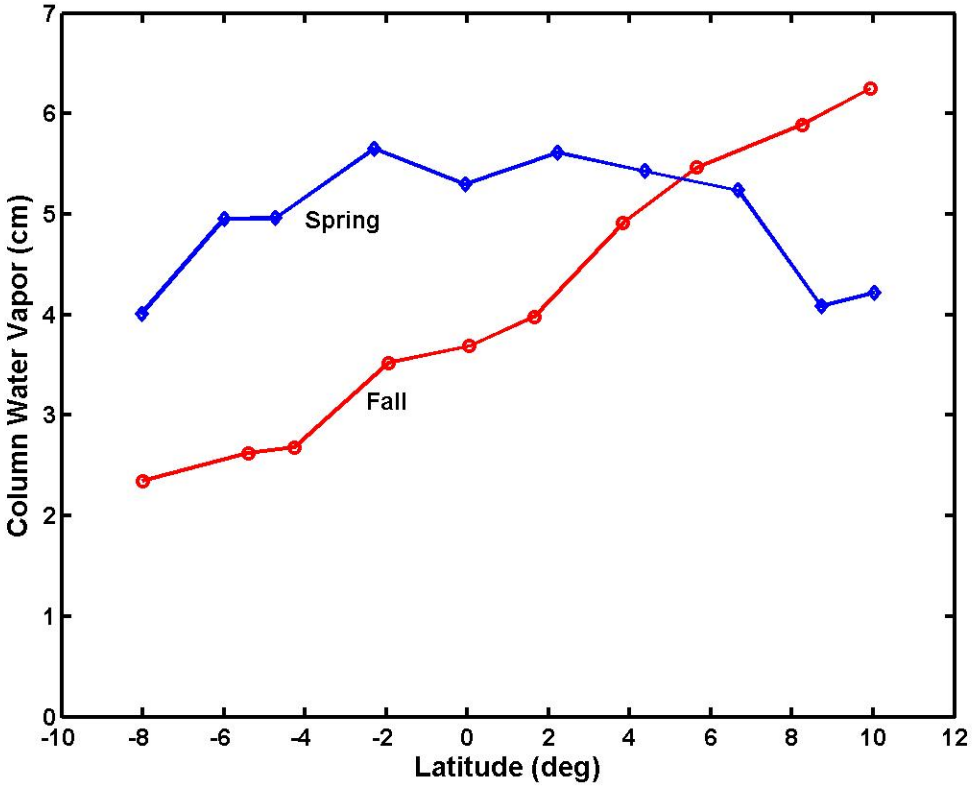
Column Water Vapor (cm)
Latitude (deg)
Spring
Fall
0
1
2
3
4
5
6
7
-10
-8
-6
-4
-2
0
2
4
6
8
10
12

(7b)

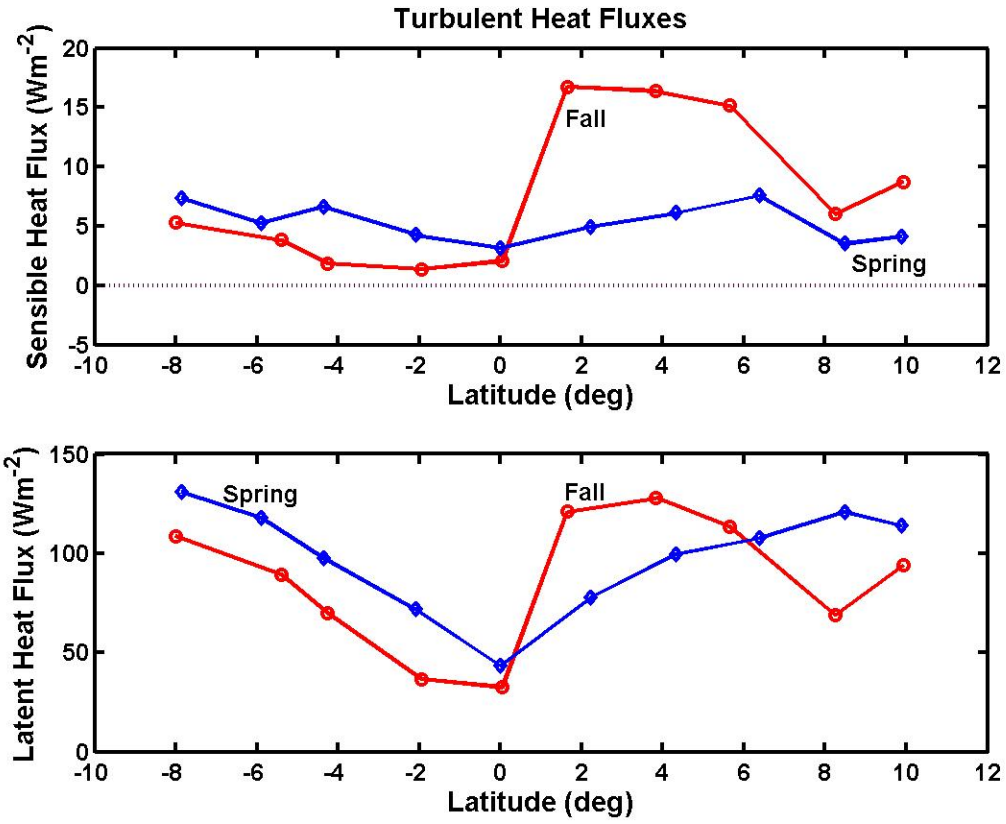

Figure 8. Latitude-averaged turbulent heat fluxes. Upper panel — sensible heat; lower panel — latent heat. Circles — fall; diamonds — spring.

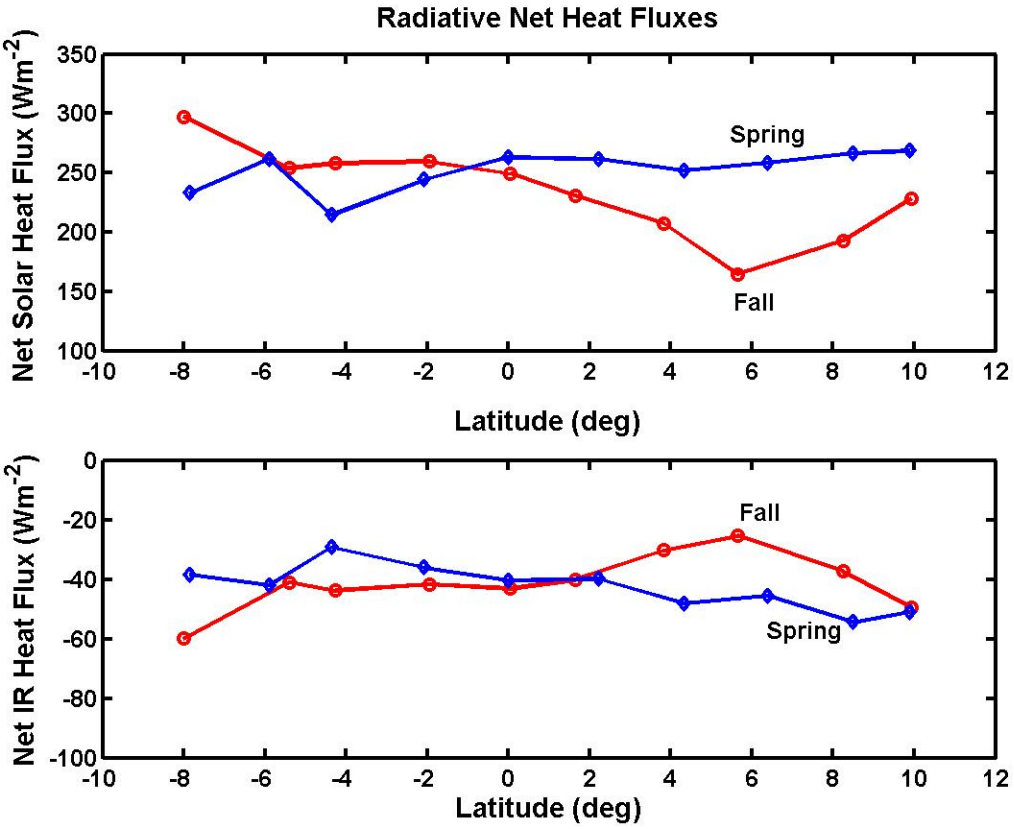

Figure 9. Latitude-averaged net radiative heat fluxes. Upper panel — solar flux; lower panel — IR flux. Circles — fall; diamonds — spring.

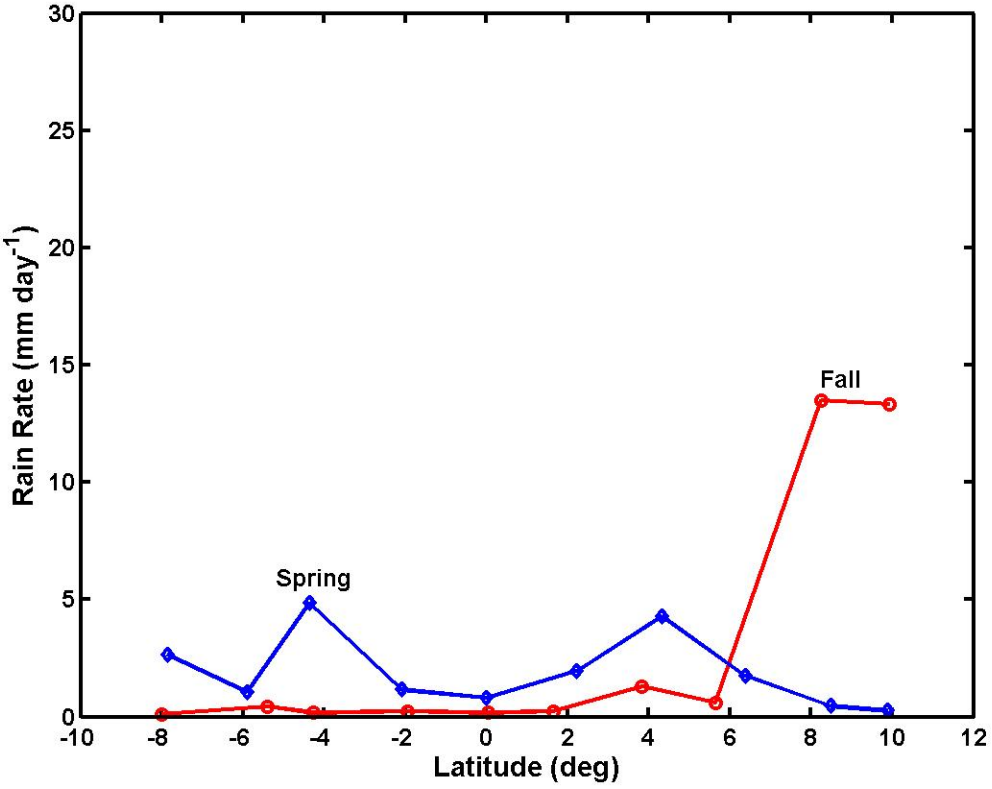

Figure 10. Latitude-averaged rain rate. Circles — fall; diamonds — spring.

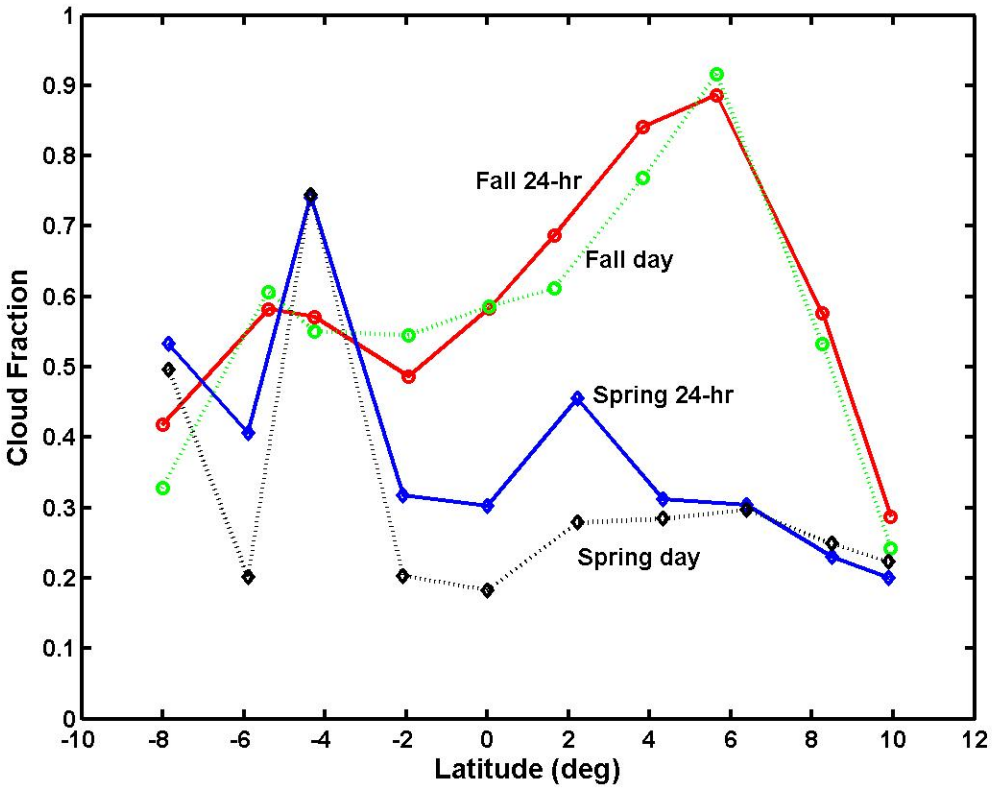

Figure 11. Latitude-averaged low cloud fraction. Circles — fall; diamonds — spring. Solid line — 24-hr average cloud fraction; dashed line — daytime average cloud fraction.

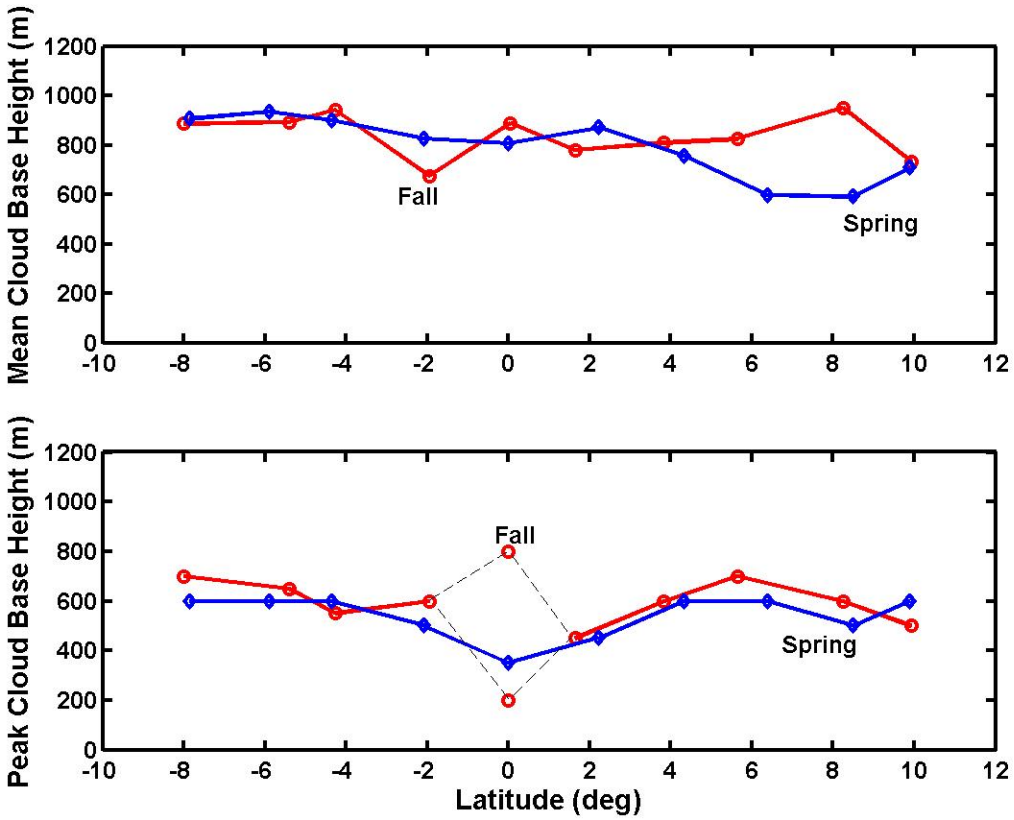

Figure 12. Latitude-averaged low cloud base heights. Circles — fall; diamonds — spring. Upper panel — mean 10-min 15% cloud base heights; lower panel — peak of the probability distribution for 10-min values. In the case of fall on the equator, there is no dominant peak and the diagram indicates the range of values.

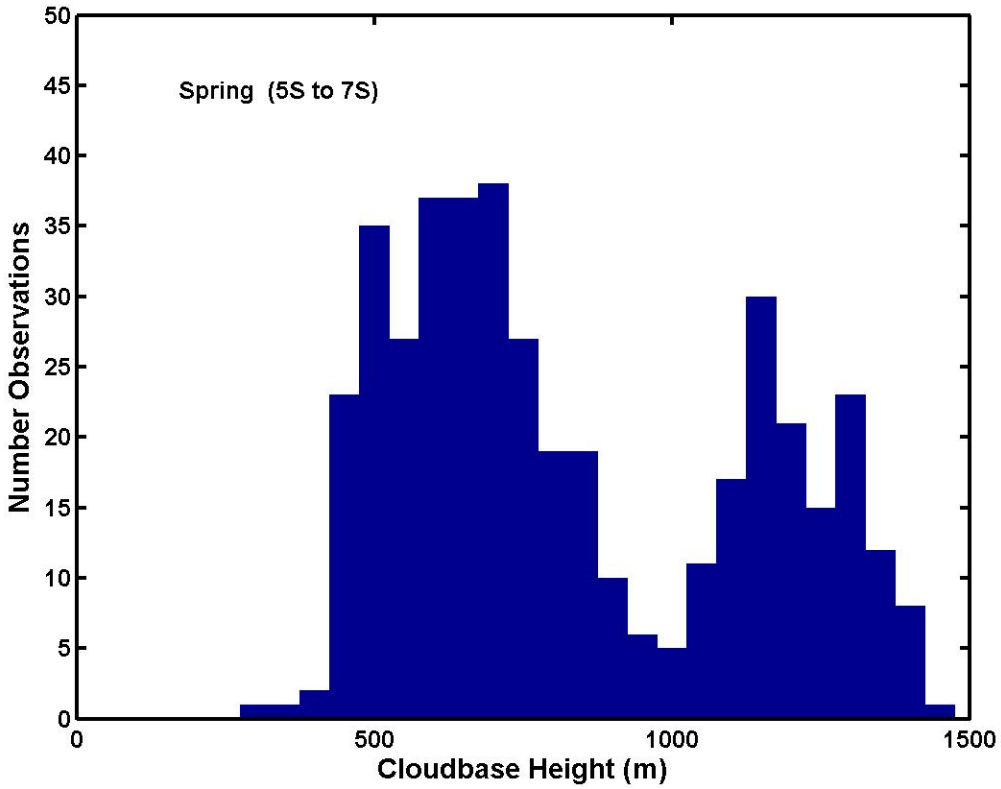

(13a)

Figure 13. Histograms of 10-min 15% cloud base heights in latitude bins: (a) spring for latitudes between 5S and 7S; (b) fall for latitudes between 1N and 1S.

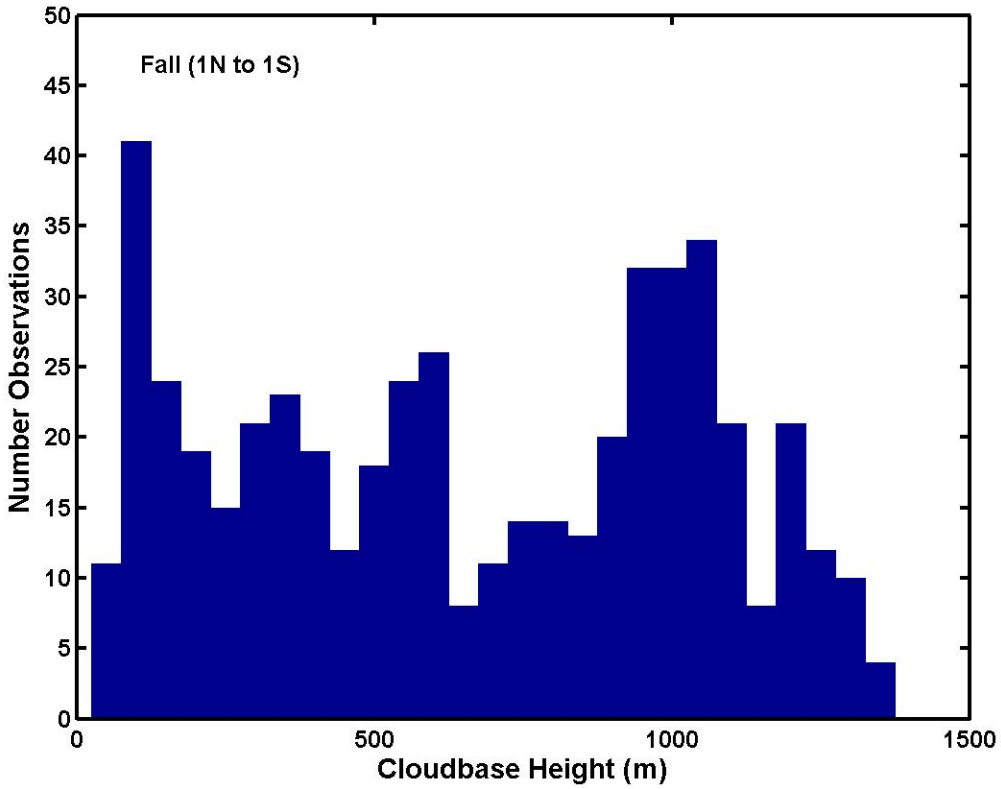
Fall (1N to 1S)
Number Observations
Cloudbase Height (m)
0
5
10
15
20
25
30
35
40
45
50
0
500
1000
1500

(13b)

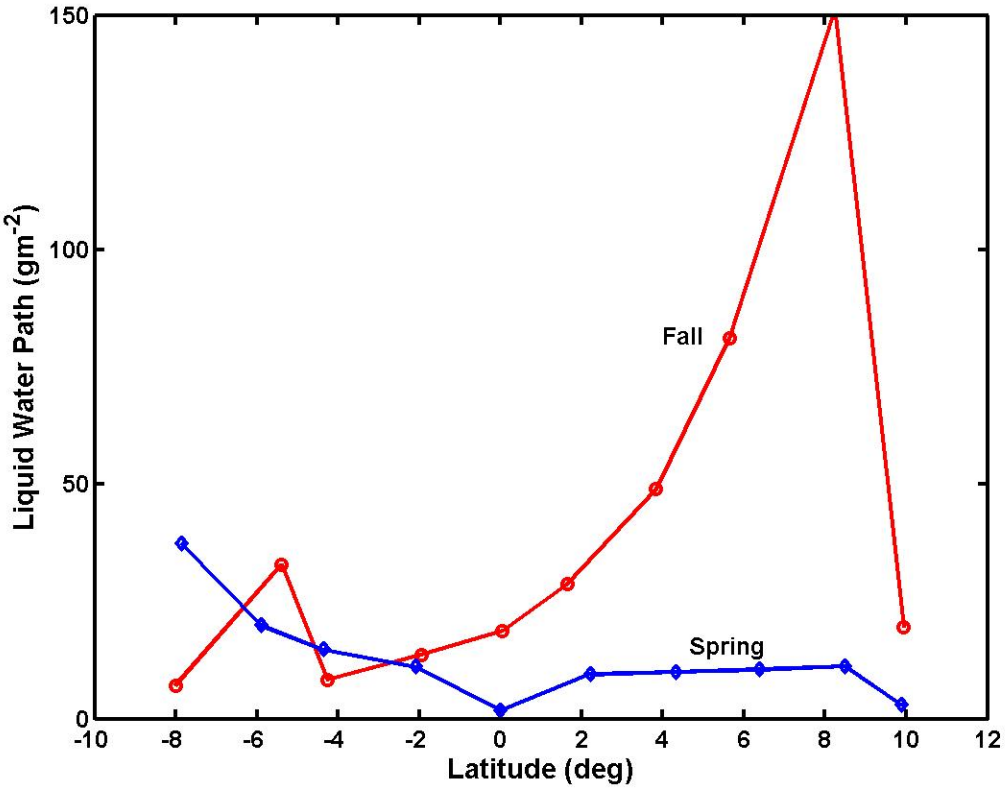

(14a)

Figure 14. Latitude-averaged cloud liquid water path: (a) mean values and (b) mean values when clouds are present. Circles — fall; diamonds — spring.

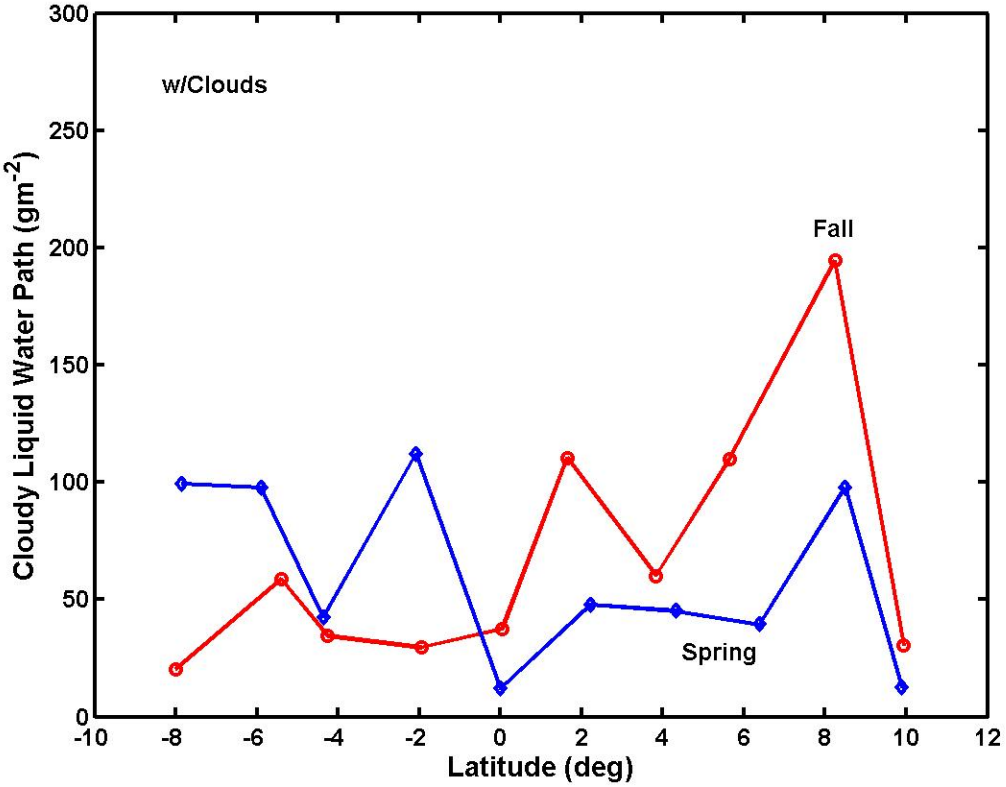
w/Clouds
Fall
Spring
Cloudy Liquid Water Path (gm-2)
Latitude (deg)
300
250
200
150
100
50
0
-10
-8
-6
-4
-2
0
2
4
6
8
10
12

(14b)

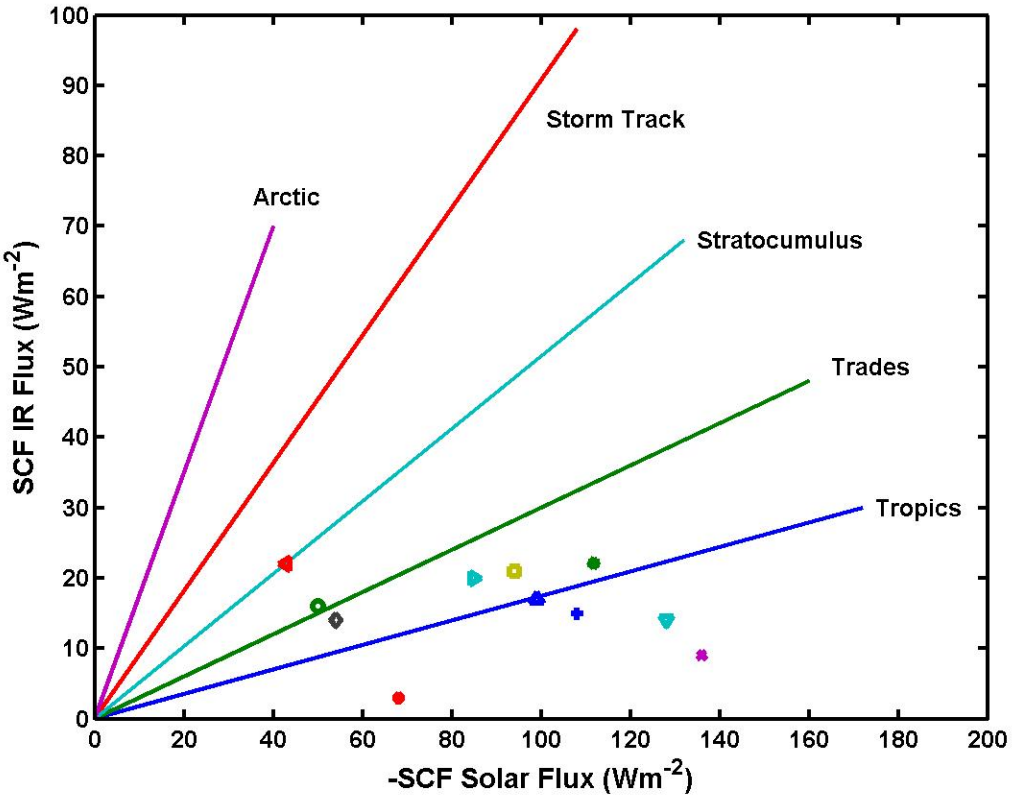

Figure 15. Cloud forcing phase diagram showing the balance of solar and IR SCF in different climate zones. An ensemble of individual days in a particular region tend to lie along a line where values near zero from small cloud fraction and values near the maximum are for cloud fraction near 1.0. The symbols represent individual cruise averages from eleven ETL cruises in the tropics. Diamond — Nauru99; plus — COARE Pilot; circle — TIWE; star — COARE1; downward-pointing triangle — COARE2; x — COARE3; square — JASMINE; upward-pointing triangle — KWAJEX1; pentagram — KWAJEX2; left-pointing triangle — PACS99; and right-pointing triangle — CSP. See Fairall et al. (2003) for definitions of the cruise names.

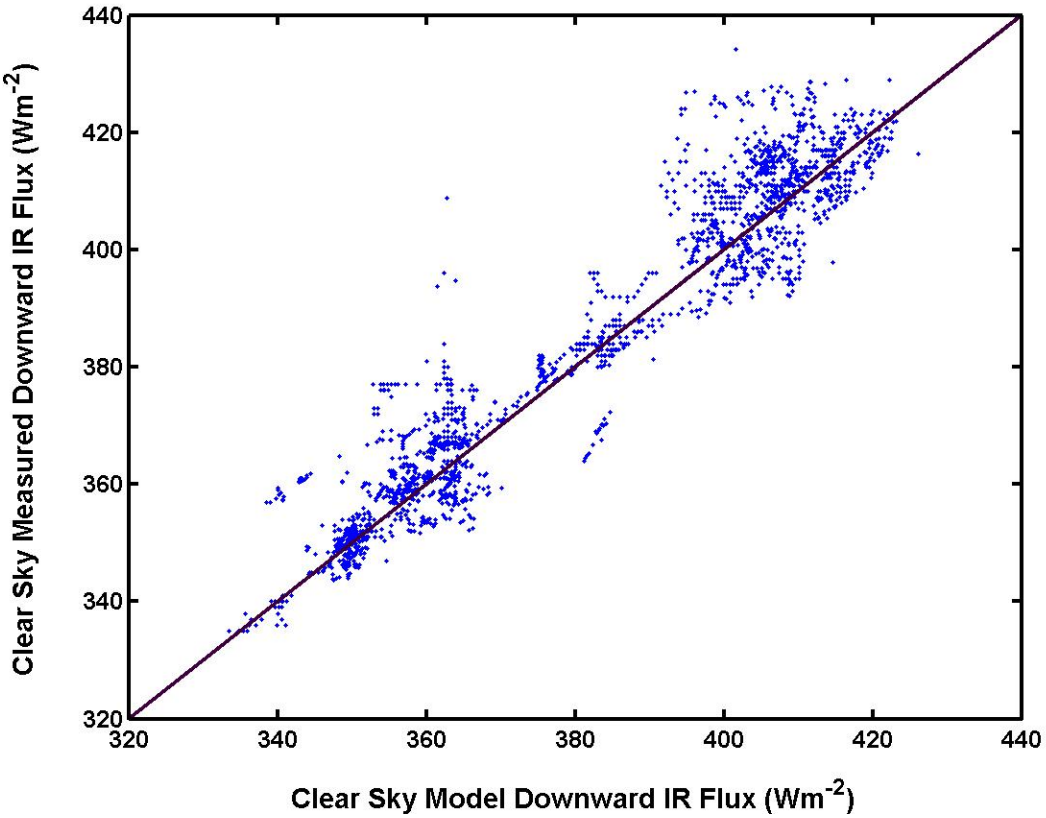

Figure 16. Comparison of clear-sky IR fluxes using model (x-axis) from Eqs. 4–5 and measurements (y-axis) for 60-min cloud free periods.

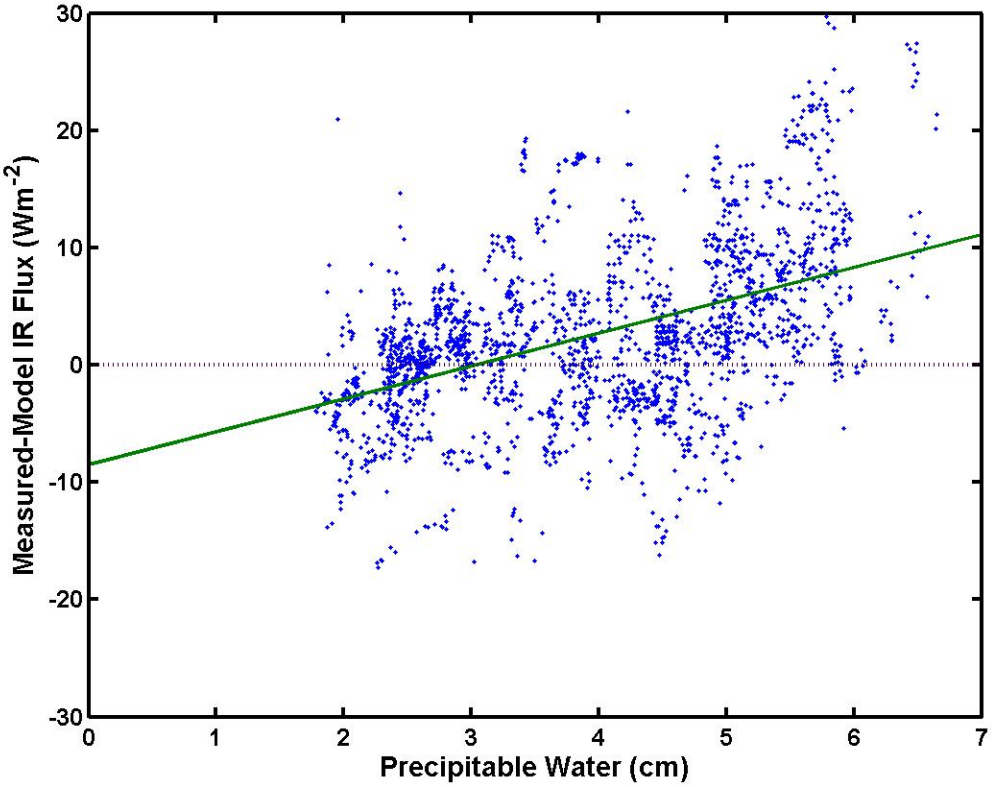

Figure 17. Measured-modeled clear-sky IR flux for 50-min cloud-free periods as a function of column integrated water vapor. Line is a linear regression.

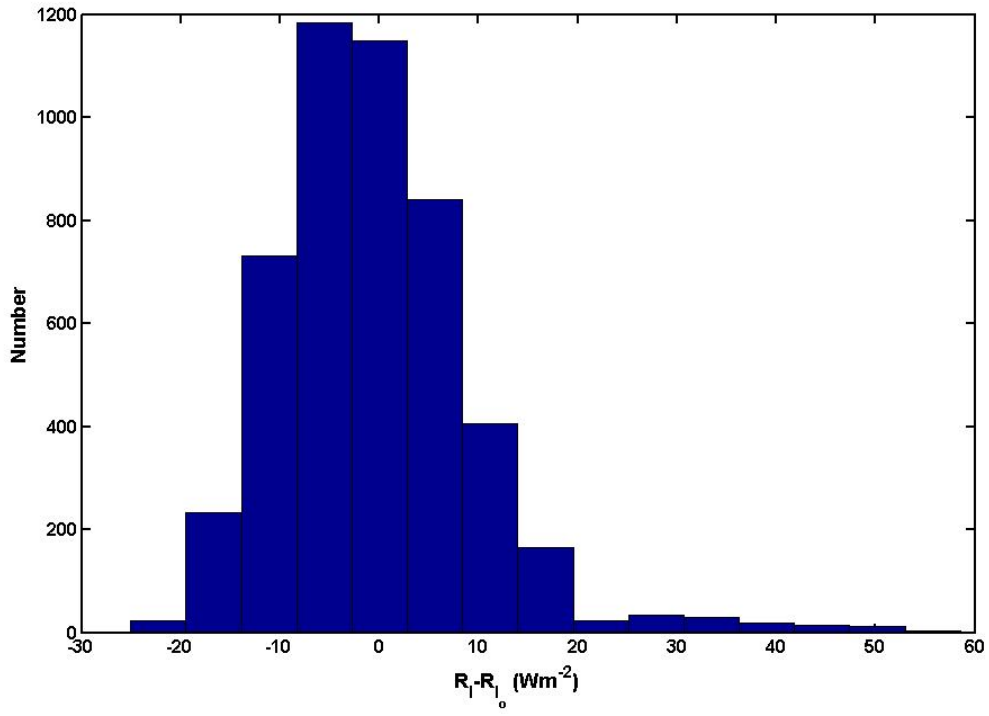

Figure 18. Measured-modeled clear-sky IR flux for 50-min cloud-free periods as a function of column integrated water vapor. Line is a linear regression.

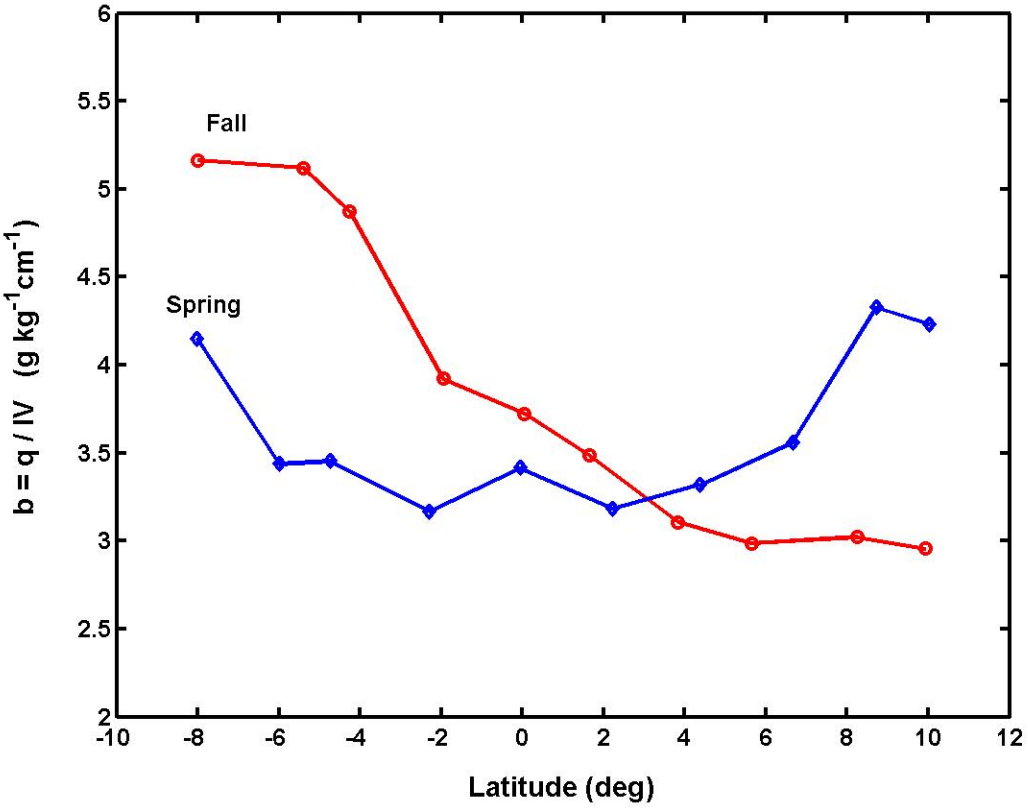

Figure 19. Ratio of latitude-averaged specific humidity to latitude-averaged column integrated water vapor. Circles — fall; diamonds — spring.

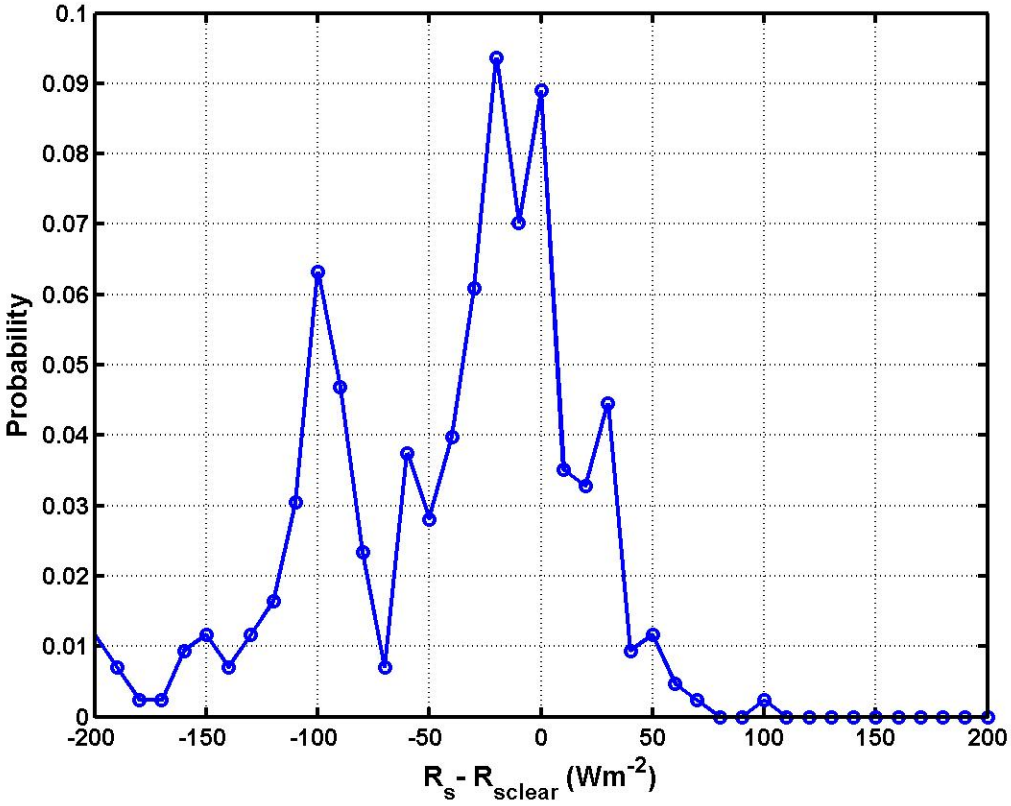

Figure 20. Probability distribution of measured-modeled clear-sky solar flux for for 50-min cloud free periods.

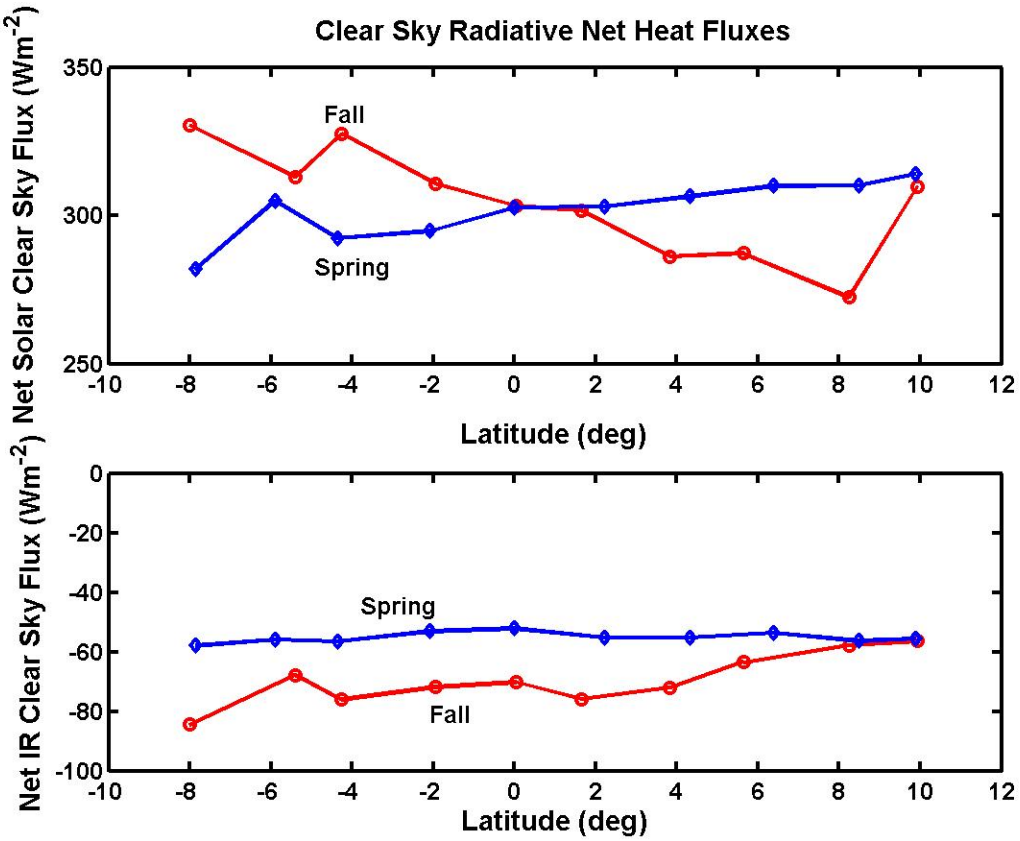

Figure 21. Latitude-averaged net clear-sky radiative heat fluxes using the models described in section 6. Upper panel — solar flux; lower panel — IR flux; circles — fall; diamonds — spring. The strange bump at 10N in the fall is caused by observations in the EPIC2001 project which occurred almost two months earlier than the typical fall monitoring cruise.

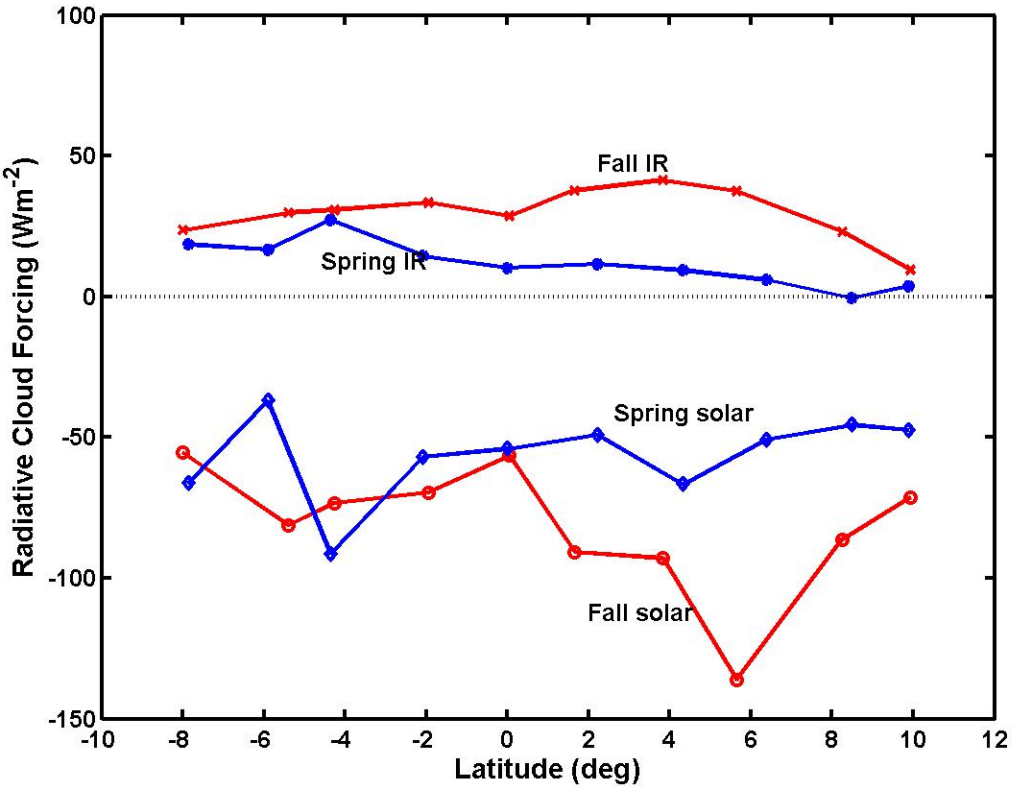

Figure 22. Latitude-averaged radiative surface CF. x — fall IR flux; closed circles — spring IR flux; open circles — fall solar flux; diamonds — spring solar flux.

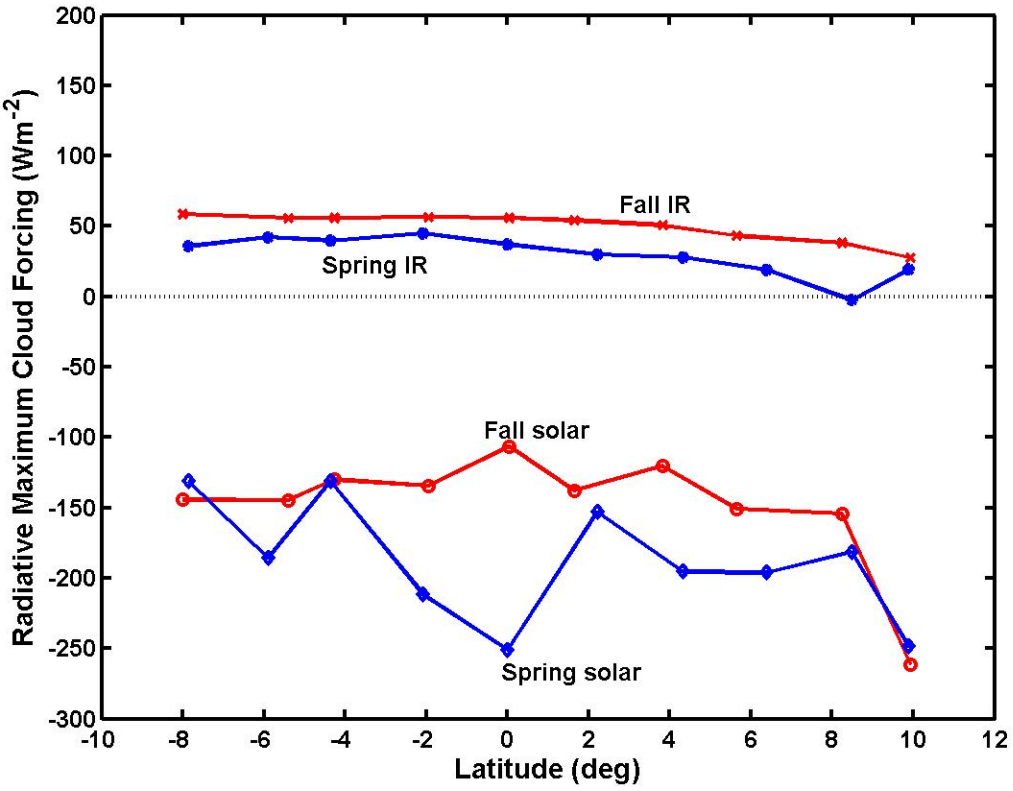

Figure 23. Latitude-averaged radiative surface maximum CF computed via Eq. 2. x — fall IR flux; closed circles — spring IR flux; open circles — fall solar flux; diamonds — spring solar flux.

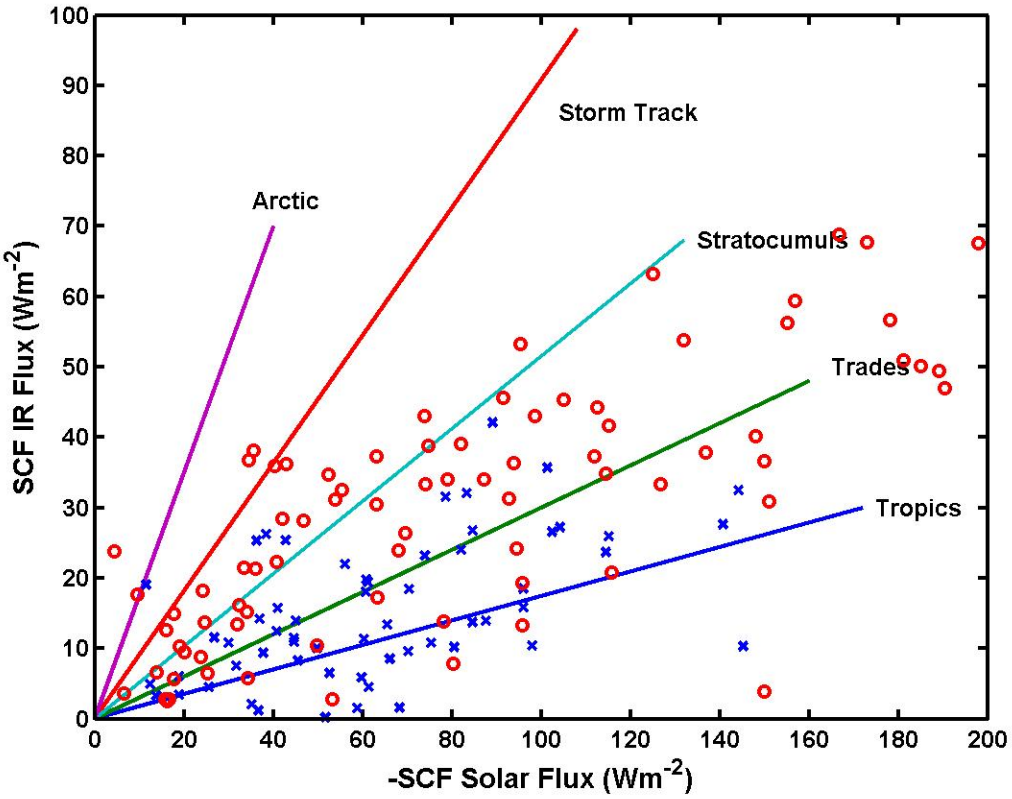

Figure 24. Cloud forcing phase diagram as in Figure 15 using daily-averaged CF values. Circle — fall; x — spring.

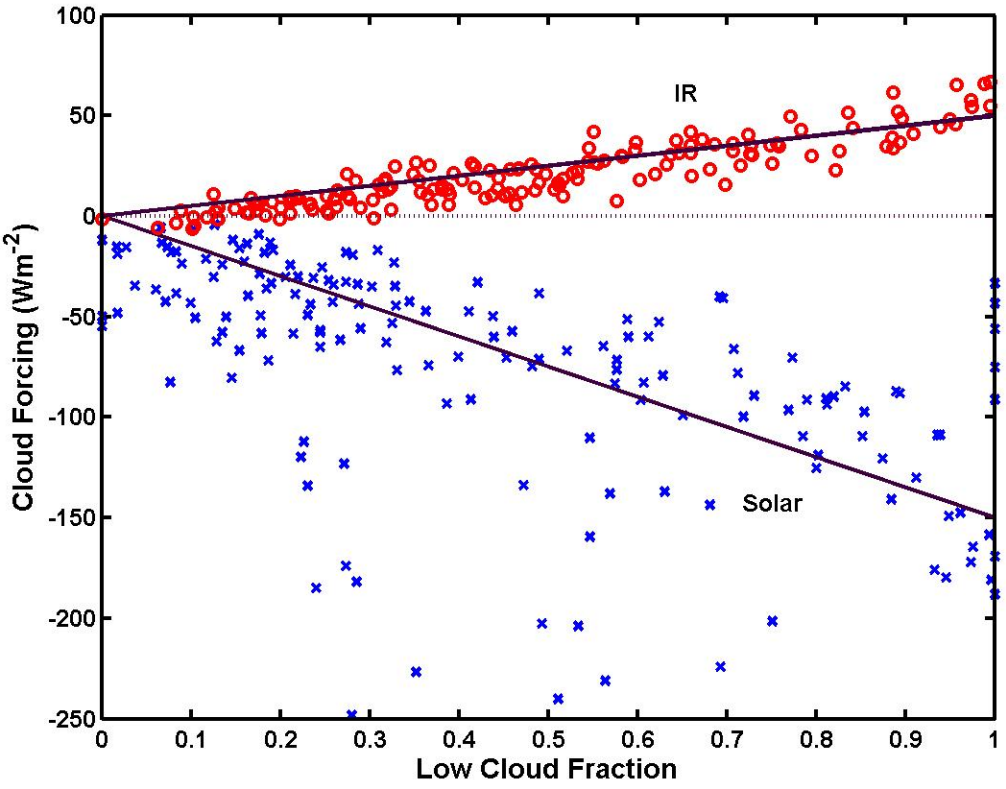

Figure 25. Daily-averaged SFC as a function of cloud fraction. Circle — IR; x — solar. The solid lines represent nominal MCF values of 50 Wm^{-2} for IR and -150 Wm^{-2} for solar fluxes.

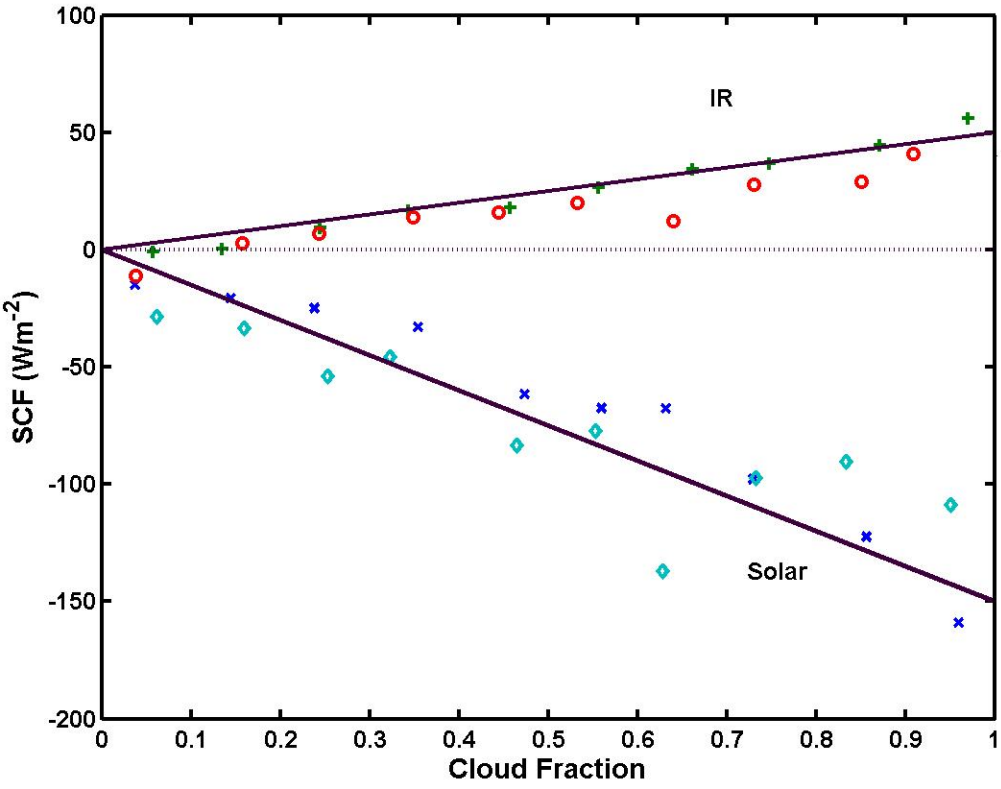

Figure 26. As in Figure 24, but the daily data have been averaged in bins of cloud fraction. Circles — spring IR; plus — fall IR; diamonds — spring solar; x — fall solar.

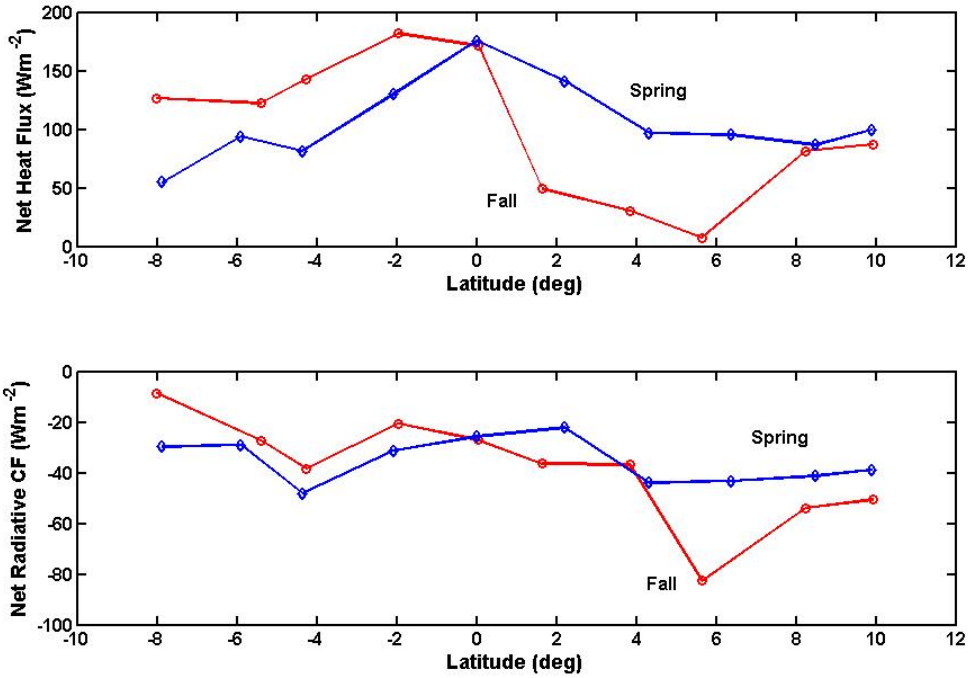

Figure 27. Latitude-averaged surface fluxes. Upper panel — net heat flux into the ocean; lower panel — contribution to the net heat flux accounted for by SCF. Circles —fall; diamonds — spring.